On the Nonlinear Aerodynamic and Stability Characteristics of a Generic Chine-Forebody Slender-Wing Fighter Configuration

Gary E. Erickson and Jay M. Brandon

June 1987

NASA

National Aeronautics and
Space Administration

On the Nonlinear Aerodynamic and Stability Characteristics of a Generic Chine-Forebody Slender-Wing Fighter Configuration

Gary E. Erickson, Ames Research Center, Moffett Field, California
Jay M. Brandon, Langley Research Center , Hampton, Virginia

June 1987

ON THE NONLINEAR AERODYNAMIC AND STABILITY CHARACTERISTICS OF A
GENERIC CHINE-FOREBODY SLENDER-WING FIGHTER CONFIGURATION

Gary E. Erickson*
NASA Ames Research Center, Moffett Field, California

Jay M. Brandon*
NASA Langley Research Center, Hampton, Virginia

Abstract

An exploratory investigation was conducted of the nonlinear aerodynamic and stability character- istics of a tailless generic fighter configuration featuring a chine-shaped forebody coupled to a slender cropped delta wing in the NASA Langley Research Center's 12-Foot Low-Speed Wind Tunnel. Forebody and wing vortex flow mechanisms were identified through off-body flow visualizations to explain the trends in the longitudinal and lat- eral-directional characteristics at extreme atti- tudes (angles of attack and sideslip). The inter- actions of the vortical motions with centerline and wing-mounted vertical tail surfaces were studied and the flow phenomena were correlated with the configuration forces and moments. Single degree-of-freedom, free-to-roll tests were used to study the wing rock susceptibility of the generic fighter model. Modifications to the nose region of the chine forebody were examined and fluid mechanisms were established to account for their ineffectiveness in modulating the highly interac- tive forebody and wing vortex systems.

Nomenclature

AR   = wing aspect ratio

b   = wing span

c   = wing root chord at fuselage-wing juncture

c_r = wing centerline chord

c_t = wing tip chord

$\bar{c}$ = wing mean aerodynamic chord

C_L = lift coefficient

$C_{L_{max}}$ = maximum lift coefficient

C_ℓ = body-axis rolling moment coefficient

C_n = body-axis yawing moment coefficient

d   = maximum forebody width

ℓ = forebody length

q_∞ = free-stream dynamic pressure

S_{ref} = wing reference area extended to the fuselage centerline

V_∞ = free-stream speed

α = angle of attack

β = angle of sideslip

Λ_{LE} = wing leading-edge sweep angle

λ = wing taper ratio

Introduction

The use of vortex flows shed from slender fuselage forebodies, wings, canards, and wing- fuselage strakes is a key element in attaining high levels of subsonic and transonic sustained and instantaneous maneuverability of advanced fighter aircraft configurations. These vortical motions induce highly nonlinear longitudinal and lateral-directional aerodynamic and stability characteristics at moderate and high angles of attack. Contributing to the complexity of the three-dimensional (3-D) flow fields are vortex trajectory asymmetries, vortex core breakdown or bursting, asymmetric breakdown, interactions of multiple vortices, and vortex flow-empennage interactions.

Present- and future-generation fighter air- craft are, and will be, operating at increasing angles of attack above maximum lift, where such nonlinear flow fields exist. The importance of understanding vortex phenomena is increased by the current trend of fighter aircraft toward shapes and concepts that are outside the established data base. The requirement for supersonic persistence will lead to wings having increased leading-edge sweep angle, and the wing-fuselage-strake blending characteristic of the F-16 will be extended for improved aerodynamic, structural, and volumetric efficiency. These factors will be conducive to increased vortex-induced effects at maneuvering angles of attack. Obtaining a working understand- ing of the principal fluid-dynamic phenomena is a necessity for the development of aircraft designs having desirable aerodynamic, stability, and con- trol characteristics. A primary objective of this study is to improve this understanding.

An experimental investigation was conducted to study the vortex flow behavior at moderate and high angles of attack of a slender, generic fighter configuration. The testing was conducted in the NASA Langley Research Center's 12-Foot Low Speed Wind Tunnel using a tailless, 60° cropped delta wing model with a chine-shaped forebody. The exploratory study expanded on the work of Erickson and Brandon[1] and increased the test data base on the nonlinear aerodynamic and stability characteristics induced by a powerful forebody vortex system that was strongly coupled to the wing vortical flow field. For comparison, testing was performed on a tangent-ogive forebody in combination with the cropped delta wing that yielded an uncoupled system of vortices. The vortex flow interactions with a centerline vertical tail and wing-mounted fins and their impact on the configuration aerodynamics and stability were evaluated. The ability of chine deflections along the nose region to modulate the forebody-wing vortical flow behavior was also assessed.

Experimental Investigation

Model Description and Test Apparatus

The wind tunnel testing was performed using the general research fighter model sketched in Fig. 1. The "tinkertoy" configuration featured a flat-plate, 60° cropped delta wing with beveled edges mounted to a main fuselage of circular cross section. The wing geometry details are provided in Table 1. The unique feature of the test model was the chine-shaped forebody. The chines extended along the length of the forebody and faired into the wing leading edges. The forebody cross-sectional shape at several longitudinal stations is depicted in Fig. 2. The design of the forebody was driven in large part by the requirement of a smooth transition to the circular main fuselage. The main intent was to design a blended forebody with fixed primary flow separation that would generate a concentrated vortex system. The chine forebody had a fineness ratio, l/d, of 3.14, where l is the forebody length extending to the strake-wing junction and d is the maximum body width.

' The forebody was instrumented with a total of 75 upper-surface, static-pressure orifices distributed in three lateral, or spanwise, rows located at 26, 50, and 73% of the forebody length measured from the nose (Stations 1, 2, and 3, respectively). The pressure orifice locations are shown in Fig. 2.

The forebody was modified to allow deflection of the chines along the nose region. The forward portion of the forebody was removable, amounting to 21% of its overall length, and separate pieces were built to provide symmetric chine deflection angles of +45° (up) and -45° (down). The alternate nose sections are illustrated in Fig. 3. The length of the deflected chines was limited to

0.21l to preserve the surface static pressure orifices at Station 1.

A tangent-ogive forebody was tested in combination with the generic fighter model to provide comparative information on uncoupled forebody and wing vortices. The uninstrumented forebody is illustrated in Fig. 1 and had a fineness ratio of 3.93. Testing was also performed on a limited basis of a hemispherical cap forebody (Fig. 1) that essentially eliminated the formation of the body vortex flows.

Two tail arrangements were investigated in conjunction with the chine forebody-cropped delta wing-fuselage model. The vertical stabilizers are depicted in Fig. 1 and featured a centerline tail and outboard-mounted fins positioned at 70% of the wing semispan.

The model six-component forces and moments were measured using an internally mounted strain-gage balance. The forebody-surface pressure measurements were obtained with a six-module Scanivalve located outside the test section. Visualization of the vortex flows was achieved by injecting smoke into the flow field using a hand-held wand.

Wind Tunnel Facility and Test Conditions

The experimental investigation was conducted in the NASA Langley Research Center's 12-Foot Low-Speed Wind Tunnel. The model with chine forebody is shown sting-mounted in the wind tunnel test section in Fig. 4. The force and moment and surface pressure measurements were obtained at a free-stream dynamic pressure (q_∞) of 5 psf (V_∞ = 65 fps), which corresponds to a Reynolds number based on the wing mean aerodynamic chord of approximately 1.1 million. Visualization of the vortex flows was performed at q_∞ = 1 psf (V_∞ = 29 fps) with a corresponding Reynolds number of 0.49 million.

The testing was divided into three phases. In the first phase, the six-component forces and moments were measured on the model with the chine, tangent-ogive, and hemispherical cap forebodies at angles of attack from 0° to 50° in 5° increments. Test runs were made at sideslip angles of 0° and +10° on the chine and tangent-ogive forebody configurations and at β = 0° with the hemispherical cap forebody. Off-body flow visualization was performed on the chine and tangent-ogive forebody arrangements at selected angles of attack and sideslip. All configurations featured the centerline vertical tail.

In the second phase, the force and moment data were obtained on the chine forebody model with centerline and wing-mounted fins. The test results were acquired at α = 0° to 50° and corresponding sideslip angles of 0° and +10°. In addition, "β-cuts" were made at selected angles of attack, where the sideslip angle was varied from -20° to +20° in 5° increments. Smoke flow

visualizations were obtained on both configurations at several angles of attack and sideslip.

The third phase consisted of six-component force and moment and forebody-surface pressure measurements on the model with the deflected chines. The quantitative data were obtained at $\alpha = 0$ to $50°$ and $\beta = 0°$ and $+10°$. Off-body flow visualization was performed on a limited basis.

Discussion of Results

Coupled and Uncoupled Forebody and Wing Vortex Systems

The model with the chine forebody is close-coupled since the strong vortex flows shed from the sharp edges of the chine and wing are highly interactive at moderate and high angles of attack. This effect is shown in the flow visualization photograph in Fig. 5 corresponding to $\alpha = 25°$ and $\beta = 0°$. By comparison, the geometry of the tangent-ogive forebody is not conducive to the development of concentrated vortex flows except at very high angles of attack where a discrete leading-edge vortex is no longer present on the wing. This configuration is uncoupled owing to the insignificant "communication" between the wing and forebody flow fields.

Off-Body Flow Visualization at $\beta = 0°$. To aid in the interpretation of the force and moment data, results from off-body flow visualizations are presented in Fig. 6, corresponding to the model with the chine and tangent-ogive forebodies. The sketches were constructed on the basis of flow-field observations, where the vortical motions were made visible by injecting smoke into the vicinity of the cores.

Distinct wing and chine forebody vortices were apparent at $\alpha = 10°$ as sketched in Fig. 6a. At this angle of attack, the vortex cores did not interact with one another. The vortices were stable along the entire wing and into the wake. In contrast, the leading-edge vortex on the wing in the presence of the tangent-ogive forebody exhibited vortex bursting near the wing trailing edge. The latter result is in reasonable agreement with existing flow visualization data obtained in water tunnels and wind tunnels on planar wings having the same sweep angle.[2]

At $\alpha = 15°$, the chine and wing vortices began to wrap around each other as shown in Fig. 6b. The vortex interaction led to some oscillation in the core behavior, but there was no evidence of flow breakdown. The model with the tangent-ogive forebody displayed a forward progression of the wing leading-edge vortex bursting to a location approximately 30% of the wing root chord ahead of the trailing edge ($x/c = 0.30$). Here, x is the distance along the chord, c, at the wing-fuselage juncture measured from the trailing edge.

The interaction of the chine and wing vortical flows was more pronounced at $\alpha = 20°$ as illustrated in Fig. 6c. As the chine vortex entered the wing flow field, it was deflected outboard and downward and eventually passed underneath the wing leading-edge vortex. The cores would then wrap around each other along the rear portion of the wing and into the wake without bursting. (Similar flow patterns were observed by Hall in water tunnel flow visualization studies[3] of chine forebodies in combination with a 55° cropped delta wing.) At the same angle of attack, the upstream traversal of the wing vortex breakdown on the tangent-ogive forebody configuration had advanced to a location approximately 65% of the wing chord from the trailing edge ($x/c = 0.65$). These results are a dramatic illustration of the "synergistic" effect associated with the favorable interaction of vortical flows. The present results are also in qualitative agreement with the water tunnel observations of Hall[3] on similar configurations having coupled and uncoupled forebody and wing vortex systems.

The interaction of the chine and wing vortices continued to increase at $\alpha = 25°$ without any evidence of core bursting over the wing surface. This effect is demonstrated in Fig. 6d. On the tangent-ogive forebody configuration, a discrete vortex core was observed only in the region of the wing apex. The flow about the upper surface of the cropped delta wing was dominated by the large, rotating flow associated with the burst leading-edge vortex.

Vortex bursting was first manifested over the wing surface on the chine forebody model at $\alpha = 30°$. This phenomenon was asymmetric, however, as the chine and wing vortices burst over the right wing while the interacting vortices on the left side remained stable into the wake as illustrated in Fig. 6e. This was a repeatable flow situation and was attributed to small forebody asymmetries and a slight roll angle of the chine component with respect to the wing plane. The core breakdown over the right wing occurred at a position approximately 50% of the distance along the wing root chord. The chine and wing vortex bursting were separate and the expanded rotating flows continued to interact, albeit to a limited extent. The vortex interaction above the left wing panel was pronounced, but less so in comparison to $\alpha = 25°$. Flow patterns consistent with the present results have been observed in wind tunnel testing of generic fighter models with chine forebodies, and specific fighter configurations with more "conventional" forebodies that employed large amounts of vortex lift (unpublished data, Northrop Corporation, Aircraft Division, 1985). In the latter studies, the angle of attack for onset of vortex breakdown at the trailing edge differed on the left and right sides with ensuing violent roll oscillations of the sting-mounted models. This phenomenon could be eliminated by increasing or decreasing the angle of attack.

At $\alpha = 30°$, the leading-edge vortex breakdown position advanced to the wing apex on the tangent-ogive forebody configuration. The smoke particles defined a large, funnel-shaped burst vortex over the entire wing surface.

The bursting of the chine and wing vortices was apparent over both wings at $\alpha = 35°$ (Fig. 6f). Symmetric core breakdown was observed at about 65% of the wing root chord from the trailing edge. Separate bursting of the wing and chine vortices was apparent and the strong interaction of the vortical flows that was evident at lower αs no longer occurred. However, side-view observations continued to show a downward displacement of the chine vortex toward the wing. An aerodynamic hysteresis effect was manifested such that pronounced asymmetries in the vortex flow field could occur depending on whether the target angle of attack was attained by coming down from a higher α or coming up from a lower model attitude. Similar effects took place at this angle of attack during a sideslip "sweep." Generally, symmetry could be achieved if sufficient time were allowed for the flow to establish itself. A large, unsteady rotating mass was developed over the wing surface in the presence of the tangent-ogive forebody.

At $\alpha = 40°$, a repeatable phenomenon characterized by symmetric vortex breakdown near the juncture of the chine and wing leading edges was observed. This flow situation is depicted in Fig. 6g. Separate and distinct breakdown of the chine and wing vortices was apparent. The flow above the wing in the presence of the tangent-ogive forebody continued to display a rotating nature, but the leading-edge vortex was completely burst. There was no indication from the smoke flow observations that the tangent-ogive forebody vortex system played an important role in the global flow field.

Longitudinal Characteristics. Figures 7 and 8 compare the lift and pitching moment characteristics of the 60° cropped delta wing model with the chine, tangent-ogive, and hemispherical cap forebodies. The higher lift and more pronounced lift-curve nonlinearity associated with the chine forebody configuration at angles of attack between 10° and 35° are apparent in Fig. 7. These effects are due to the development and favorable mutual interaction of the chine and wing vortical motions within this range of the angle of attack. The increased lift curve slope at $\alpha = 10°$ marks the emerging influence of the chine forebody and wing vortices in the configuration flow field. The inflection in the lift curve at $\alpha = 15°$ coincides with the onset of strong interaction between the chine and wing vortical flows and the increased vertical displacement of the interacting vortex systems from the wing upper surface. Maximum lift is achieved at $\alpha = 30°$, where vortex bursting, albeit asymmetric, first appears over the wing.

The local lift-curve slope reduction at $\alpha = 10°$ for the configurations with the tangent-ogive and hemispherical cap forebodies is associated with the onset of vortex bursting near the wing trailing edge. Maximum lift is achieved at $\alpha = 30°$ where the burst position of the leading-edge vortex is at, or near, the wing apex. These results are similar to data obtained by Wentz[4] on delta wings encompassing a range of sweep angle. It was observed that delta wings having sweep angles of 70° or less attained maximum lift when vortex bursting reached the apex. On the more highly swept planforms, where the vortex lift represented a larger percentage of the total lift (similar to the chine forebody configuration), maximum lift occurred when core breakdown first appeared at the wing trailing edge.

The small contribution of the tangent-ogive forebody to the overall lift at angles of attack up to 35° can be seen by comparison to the hemispherical cap results in Fig. 7.

The larger projected planform area of the chine forebody results in a slight increase in the pitch instability at low lift levels as shown in Fig. 8. The unstable "break" in the pitching moment curve at $C_L \doteq 0.80$ is the result of the strong interaction of the chine forebody and wing vortices and the subsequent upward movement of the vortex system along the rear portion of the wing. At higher C_Ls, the increasing magnitude of the chine forebody vortex lift, which acts far ahead of the center of gravity, contributes to the large increase in the pitch instability. Finally, the unstable stall is caused by the onset of the chine-wing vortex system breakdown near the wing trailing edge and the maintenance of a concentrated vortex along the forebody.

Off-Body Flow Visualization in Sideslip. The sketches in Figs. 9-12 show the effect of sideslip on the vortex flow patterns observed in smoke flow visualizations of the chine and tangent-ogive forebody configurations at selected angles of attack. The results will be useful in the ensuing discussion of the lateral-directional characteristics.

Figure 9 illustrates the vortex core path and breakdown characteristics at $\alpha = 20°$ and $\beta = 0°$, 5°, and 10°. The sensitivity of the chine and wing vortices to the sideslip angle is readily apparent in the sketches. In comparison to the stable vortical flows at $\beta = 0°$, a sideslip angle of 5° promoted bursting of the windward chine-wing vortex system at about 50% of the distance along the wing root chord measured from the trailing edge. The vortices did not wrap around each other as in the $\beta = 0°$ case, although the chine vortex displayed a marked outboard deflection toward the wing vortex prior to bursting. The flow in the vicinity of the centerline tail was not adversely affected since the bursting occurred at a position sufficiently outboard on the wing. The interaction of the leeward chine and wing vortices

diminished and the vortex cores displayed a vertical displacement from the wing upper surface in comparison to the result at $\beta = 0°$. At $\beta = 10°$, the windward chine and wing vortex cores exhibited separate bursting at a location about 65% of the wing root chord from the trailing edge. The windward chine vortex moved inboard toward the forebody surface and was effectively captured in the "cusp-shaped" region. The reduced-energy wake from the wing passed the vertical tail, although the latter was not immersed in the burst rotating flow. Increased sideslip caused a corresponding increase in the separation distance between the leeward chine and wing vortices to the extent that the wrapping-around of the vortex cores was eliminated. The forebody vortex moved outboard of the chine edge prior to passing over the wing surface. The upward vertical displacement of the vortex flows, particularly the chine vortical motion, was pronounced at this sideslip angle. The sensitivity of the vortex interactions and core breakdown to the sideslip angle is consistent with the water tunnel observations of Hall.[3]

The configuration with the tangent-ogive forebody also exhibited marked vortex core positional and breakdown asymmetries due to sideslip. The forward advance of the windward wing leading-edge vortex burst position toward the apex and the concurrent downstream displacement of the leeward vortex breakdown are clearly shown in Fig. 9. At $\beta = 10°$, a large funnel-shaped rotating flow was apparent on the windward wing that passed the vertical tail. On the leeward side, the wing vortex was stable into the wake and moved outboard and upward relative to $\beta = 0°$.

Figure 10 depicts the observed flow patterns at $\alpha = 25°$. The coupled vortex system on the chine forebody configuration continued to display a marked sensitivity to the sideslip angle. The highly interactive and stable vortex cores that were apparent at $\beta = 0°$ became uncoupled and unstable on the windward wing at $\beta = 5°$. Separate bursting of the chine and wing vortices occurred at about $x/c \doteq 0.65$ and the low-energy wake associated with the burst vortex system was observed to hit the vertical tail. Smoke that was injected into the windward wing flow was also observed to carry over onto the leeward side. The chine vortex remained "captured" within the concave region of the forebody. The interaction of the vortex cores was noticeably reduced on the leeward side in comparison to $\beta = 0°$. The outboard deflection of the chine vortex was diminished as it passed over the wing. In addition, the core paths did not intersect until the trailing edge region as opposed to mid-chord at $\beta = 0°$. The effect of sideslip on the chine forebody configuration flow field was more pronounced at $\beta = 10°$. Bursting of the windward vortices occurred near the chine-wing juncture. However, the chine-shaped forebody was still able to develop and sustain a concentrated vortex within the cusp-shaped region. The smoke particles

within the burst vortex system revealed a large region of reverse flow over the wing. The flow visualizations also clearly showed the large rotating mass from the wing impinging on the centerline tail. On the leeward side, there was no interaction of the chine and wing vortices. In the planview, the forebody vortex moved far outboard of the chine, while the wing vortex moved closer to the leading edge. In the sideview, the vortices were displaced vertically from the wing. This was particularly pronounced for the chine forebody vortex owing to the decoupling from the wing flow field.

The tangent-ogive forebody configuration displayed a forward advance of the leading-edge vortex bursting to the apex of the windward wing when the sideslip angle was increased from 0° to 5° at $\alpha = 25°$. A large, funnel-shaped breakdown region was apparent over the wing surface. There was no evidence, however, that the vertical tail was immersed in this flow. A marked increase in the stability of the leeward wing vortex occurred such that bursting was displaced downstream to $x/c \doteq 0.50$. At $\beta = 10°$, the windward wing exhibited massive flow breakdown. Within the burst vortex, the smoke particles revealed unsteady, predominantly reverse flow. The separated wing wake clearly impinged on the vertical tail at this sideslip angle. On the leeward side, the wing vortex moved outboard and was in the vicinity of the wing leading edge. However, the core and its breakdown position were oscillatory.

At $\alpha = 30°$ and $\beta = 5°$, the windward chine and wing vortices burst near the forebody-wing juncture as sketched in Fig. 11. Smoke particles from the burst vortex system passed over the top of the main fuselage and onto the leeward side. The centerline vertical tail was blanketed by the low-energy wake from the windward wing. A discrete chine vortex core was observed in proximity to the windward forebody surface. On the leeward side, the upward movement of the vortex cores was apparent and the intersection of the chine and wing vortex paths was displaced downstream to the wake region. The entire windward wing was dominated by the burst vortex system at $\beta = 10°$ and the centerline tail was enveloped in this uncontrolled separated flow region. A concentrated vortex core was maintained within the windward cusp of the chine forebody. The leeward forebody vortex moved upward and outboard of the cusp region and its influence on the forebody flow was correspondingly reduced. The vertical displacement of the chine vortex core was sufficient to decouple it from the wing vortical flow.

The funnel-shaped burst vortex that was apparent at $\alpha = 30°$ and $\beta = 0°$ on the cropped delta wing of the tangent-ogive forebody configuration was altered to a massive, unsteady separated flow region on the windward side at $\beta = 5°$. This flow, in turn, hit the vertical tail surface. On the leeward wing, a discrete leading-edge vortex core was observed with a breakdown position at

approximately 65% of the wing root chord from the trailing edge. The windward wing was completely stalled at $\beta = 10°$ and the vertical tail was blanketed by the ensuing wake. A wildly oscillating leading-edge vortex core was visualized above the leeward wing with a mean burst position at about 30% of the root chord measured from the trailing edge. A leeward forebody vortex was also seen that was positioned at a considerable distance from the wing upper surface.

Figure 12 illustrates the vortex flow patterns at $\alpha = 35°$. At $\beta = 5°$, the windward chine and wing vortex breakdown advanced to a position upstream of the forebody-wing junction. The wing was dominated by the greatly expanded burst vortical flow, which enveloped the vertical tail. Discrete forebody and wing vortices were evident on the leeward side, and these vortical flows burst in an unsteady fashion in the near-wake region. At $\beta = 10°$, the breakdown of the windward vortex system moved upstream to a location over the chine-shaped forebody. The smoke entrained into the burst vortex revealed highly unsteady, reverse flow above the wing, and the tail surface was blanketed by the windward wing wake. There was also a significant carryover of smoke from the windward to the leeward sides. In the planview, the leeward forebody vortex was displaced outboard of the chine edge along a large percentage of the forebody length, whereas the wing vortex moved closer to the leading edge. The latter exhibited core oscillations near the wing trailing edge. In the sideview, the vortices were positioned far above the model surface. Furthermore, the cores were sufficiently far apart that there was no interaction at any point in the flow field.

At $\alpha = 35°$, the tangent-ogive forebody configuration displayed complete stall of the windward wing at $\beta = 5°$ and the vertical tail was blanketed by the low-energy wake. A discrete, but oscillatory, vortex core was visualized along approximately the forward 30% of the leeward wing, whereupon the core flow broke down. At $\beta = 10°$, the smoke that was injected into the apex region of the windward wing was entrained into the leeward flow field. The leeward wing leading-edge vortex core was well-defined to $x/c \doteq 0.30$, but the core and breakdown were very unsteady.

Lateral-Directional Characteristics. Figure 13 compares the variation of the rolling-moment coefficient, C_ℓ, with the angle of attack at $\beta = 10°$ obtained on the model with the chine and tangent-ogive forebodies. Both configurations incorporate the centerline vertical tail. The rolling moment trends are similar for the coupled and uncoupled forebody-wing arrangements. Specifically, each displays increasingly stable values of C_ℓ as the angle of attack is increased from low to moderate values. The maximum value of the stable rolling moment is limited, however, by the onset of vortex breakdown over the windward wing. As a result, the configurations attain a

C_ℓ peak with a further increase in α. The abrupt decrease in the rolling moment coefficient leading to a minimum $|C_\ell|$ is typical of fighter configurations that employ vortex lift. This trend marks the appearance of severe vortex positional and burst asymmetries caused by sideslip. This is followed by a recovery to large stable values of the rolling moment coefficient. The following paragraphs provide a more detailed discussion of the major lateral aerodynamic data trends.

The model with the chine-shaped forebody exhibits large, stable rolling-moment increments at angle of attack less than 30° relative to the tangent-ogive forebody configuration. This is due to the development of concentrated chine and wing vortices and their favorable interaction which lead to greater vortex-induced lift and delayed onset of vortex breakdown asymmetry. The flow sketches in Fig. 9 corresponding to $\alpha = 20°$ and $\beta = 10°$ showed less severe effects of vortex breakdown over the windward wing of the chine forebody configuration. This accounts for the more stable C_ℓ values for the coupled forebody-wing arrangement. It is interesting that the rolling-moment coefficient at this angle of attack is stable, despite the large degree of vortex positional and bursting asymmetries exhibited by both configurations. The induced effects of the burst vortex on the windward wing are sufficiently large to overcome the corresponding effects of the more stable leeward vortical flows, which are weaker and displaced vertically from the wing surface.

At $\alpha = 25°$, both configurations develop a minimum $|C_\ell|$. The corresponding flow patterns at $\beta = 10°$, shown previously in Fig. 10, were similar. Namely, the windward wing was characterized by a large, slowly rotating mass within which existed an extensive region of reverse flow. The resultant lift loss was sufficient to promote the "trough" in the C_ℓ versus α curve. The flow-field observations revealed a somewhat more energetic flow about the windward wing of the chine forebody configuration, which is consistent with the stable C_ℓ increment with respect to the tangent-ogive forebody model at this angle of attack.

At $\alpha = 30°$, the chine and tangent-ogive forebody configurations exhibit a recovery to stable rolling-moment coefficients of comparable magnitude. This effect occurs despite the advancing stall of the windward wing on both configurations. The rolling moment recovery is associated with the significant upward displacement of the leeward vortices and, as a result, decreased vortex-induced lift on the leeward wing panel. The more pronounced recovery of the tangent-ogive forebody model is attributed to the onset of leading-edge vortex bursting over the leeward wing, which was sketched in Fig. 11.

The yawing moment coefficient (C_n) variation with the angle of attack at $\beta = 10°$ is presented in Fig. 14. The chine and tangent-ogive forebody configurations display large, stable yawing moments at low and moderate angles of attack followed by a marked decrease to unstable C_n values at higher αs. The centerline vertical tail is the primary contributor to the nearly constant, stable yawing moments at $\alpha = 0°$ to 15° on the model with the tangent-ogive forebody. As the angle of attack is increased from 15°, the advance of leading-edge vortex bursting on the windward wing and the associated larger wake in proximity to the tail surface is responsible for the departure from the uniform C_n values. The expanded, low-energy wake from the windward wing hits the empennage at $\alpha = 25°$, as presented in the flow sketches in Fig. 10 corresponding to $\beta = 10°$. This results in a loss of tail effectiveness and the ensuing abrupt decrease to large, unstable C_n values at angles of attack from 25° to 40°. The development of a strong forebody vortex system, that is uncoupled from the wing flow field, is responsible for the large, restoring yawing moments at angles of attack beyond 40°.

At angles of attack between 0° and 20°, the chine forebody configuration develops increasingly stable yawing moments that greatly exceed the C_n values obtained with the tangent-ogive forebody model. The chine forebody augments the centerline vertical tail contribution to the yaw stability. Flow-field observations in the present study and surface static pressure measurements obtained in Ref. 1 revealed the development of a concentrated vortex within the windward cusp of the chine forebody component. The vortex strength and, hence, the suction pressures on the lateral-facing surface of the forebody that contribute to the restoring yawing moments, increased with the angle of attack. In a manner similar to the tangent-ogive forebody configuration, the chine forebody model displays a sudden decrease in the yawing moment coefficient as the angle of attack is increased from 20°. The flow patterns at $\alpha = 25°$ and $\beta = 10°$ sketched in Fig. 10 showed the low-energy wake from the windward wing enveloping the centerline tail with an ensuing loss in the tail effectiveness. The C_n values remain stable, however, up to an angle of attack of at least 35°. This reflects the ability of the chine forebody to develop and sustain a concentrated vortex within the channel formed by the blended geometry. The yawing moment coefficient displays a second, pronounced decline from stable to large, unstable values beginning at $\alpha = 30°$. This trend is attributed to the advance of vortex bursting over the windward chine forebody surface, which was illustrated in the flow patterns in Fig. 12.

Centerline Tail Versus Wing-Mounted Vertical Fins

Off-Body Flow Visualization at $\beta = 0°$.
Figure 15 presents sketches, based on smoke flow visualizations, of the chine-wing vortex patterns in the presence of the centerline and outboard-mounted vertical stabilizers. The sketches in Fig. 15a, corresponding to an angle of attack of 20°, reveal a stable, highly interactive chine-wing vortex system on the model with the centerline vertical tail. The results obtained with the wing-mounted fins, however, indicate that the stabilizer was in the path of the interacting chine and wing vortices and, consequently, promoted breakdown of the core flow. The chine-wing vortex interaction and vortex-fin interaction were complex phenomena. The chine vortex was deflected sharply outboard and downward as it interacted with the wing vortical flow. A helical pattern composed of two distinct vortex cores was formed. The chine vortex bent streamwise and passed over the wing leading-edge vortex along the rear portion of the wing to a position in proximity to the inboard surface of the fin. The pressure field imposed by the fin was sufficiently adverse to promote bursting of the chine vortex upstream of the trailing edge. The wing vortex, as it passed underneath the chine vortical flow, was deflected outboard toward the fin and subsequently burst at the fin just upstream of the chine vortex breakdown position. The vortex core paths and breakdown position were oscillatory in the region of the fin, and the vortex pattern presented in Fig. 15a was a mean flow condition.

Figure 15b compares the observed flow patterns at $\alpha = 25°$. The model with the centerline tail continued to develop a stable, strongly coupled chine-wing vortex system. The wing-mounted fin configuration was again characterized by vortex bursting in the vicinity of the stabilizer and this flow situation is illustrated in the smoke flow visualization photograph in Fig. 16. The interaction of the chine and wing vortices was less pronounced relative to $\alpha = 20°$. In addition, there was an asymmetry of the vortical flow fields from the left to right sides. Upstream of the left-hand fin, the chine vortex was deflected outboard and downward underneath the wing leading-edge vortex in a manner similar to the result at $\alpha = 20°$. As the chine vortex continued its helical path, it was displaced upward and passed over the top of the fin. This was followed by core bursting near the trailing edge. The wing vortex exhibited a separate breakdown on the inboard side of the fin slightly upstream of the forebody vortex burst point. On the right-hand side, distinct breakdown of the chine and wing vortices was observed at the inboard fin surface. It was inferred from the smoke flow visualizations that the unsteady burst vortices induced a severe fin buffet environment at this angle of attack.

At $\alpha = 30°$, the model with the centerline vertical tail displayed a significant vortex asymmetry as illustrated in Fig. 15c. The wing-mounted fin arrangement was characterized by symmetric breakdown of the chine and wing vortices at approximately the same location ($x/c \doteq 0.50$) as the right-hand side of the centerline tail

configuration. The helical interaction pattern of the chine and wing vortices was absent at this higher angle of attack. The vortices continued to exhibit separate and distinct core breakdown. The smoke particles within the burst vortex system revealed highly unsteady flow in the vicinity of the fins.

The vortex behavior at $\alpha = 35°$ was similar for the centerline and wing-mounted tail configurations as depicted in Fig. 15d. The flow was characterized by symmetric bursting of the chine and wing vortices at approximately 65% of the wing root chord measured from the trailing edge.

Longitudinal Characteristics. Figure 17 compares the lift characteristics with the centerline vertical tail and wing-mounted fins. The lift is comparable at angles of attack up to 5°, where the vortex flows are insignificant. As the angle of attack is increased from 5°, the chine and wing vortices increase in size and strength to become a dominant feature of the wing flow field. The effect of the wing-mounted fins is to significantly decrease the lift at angles of attack from approximately 10° to 30° in comparison to the data obtained on the centerline tail configuration. This is due to the advanced breakdown of the chine and wing vortices that was illustrated in the flow patterns in Figs. 15a-c. At angles of attack of 35° and greater, the lift characteristics are similar. This is consistent with the flow field observations in Fig. 15d, which showed comparable chine-wing vortex burst positions at $\alpha = 35°$ on both configurations. At angles of attack beyond maximum lift, the streamwise pressure gradient on the wing without fin is sufficiently adverse to promote vortex bursting at a position far upstream of the trailing edge. The installation of wing-mounted fins within the large-scale region of flow separation has little effect, therefore, on the vortex breakdown behavior.

The configuration with the wing-mounted fins exhibits increased pitch instability in comparison to the model with the centerline vertical tail. This effect is shown in Fig. 18. The advanced vortex bursting caused by the fins reduces the lift over the rear portion of the wing and, as a consequence, promotes large nose-up pitching increments. The pitching moments beyond maximum lift are comparable because of the similar flow-field characteristics.

Off-Body Flow Visualization in Sideslip. Figures 19 and 20 present sketches of the vortex flow patterns about the centerline vertical tail and wing-mounted fin configurations at selected angles of attack and sideslip. The flow-field observations at $\alpha = 30°$ and 35° indicated that the forward advance of the windward chine and wing vortex bursting as the sideslip angle was increased from 0° was similar on both tail arrangements. These results indicate that the presence of the fins had a nominal effect on the

vortex behavior at these angles of attack and sideslip. It was apparent that the windward fin was immersed in the unsteady burst vortex system. Although flow-field information in sideslip was not obtained on the twin-tail configuration at lower values of α, it is surmised from the $\beta = 0°$ results that the windward fin was positioned in an unfavorable flow field over a wide range of the angle of attack. The centerline vertical tail, on the other hand, was not visibly affected by the windward vortex bursting until $\alpha = 25°$ (Fig. 10).

The leeward vortical flows on the centerline and outboard fin arrangements displayed similar trends due to sideslip. Namely, the interaction between the chine and wing leading-edge vortex cores was reduced and, subsequently, eliminated as the sideslip angle was increased. In addition, the stability of the vortex system was enhanced concurrently with an outboard and upward displacement of the cores. The leeward fin was "bounded" by the wing and chine vortices, which were positioned outboard and above the stabilizing surface, respectively. The fin appeared to displace the chine vortex away from the wing upper surface. Vortex bursting did not occur over the leeward wing surface on either configuration at $\alpha = 30°$ and 35°, although core oscillations were apparent. The smoke flow visualizations suggested that sideslip improved the flow about the leeward wing-mounted fin at these angles of attack. It is noted that the hysteresis that was observed on the model with the centerline tail was not apparent on the twin-tail configuration.

Longitudinal and Lateral-Directional Characteristics. Figure 21 presents the variation of the lift coefficient with sideslip at $\alpha = 20°$ to 35° for the centerline tail and wing-mounted fin configurations. Both exhibit a lift decrease with sideslip at angles of attack from 20° to 30° (Figs. 21a-c). At $\alpha = 20°$ (Fig. 21a), the lift loss due to sidelip is largely promoted by the forward advance of the chine-wing vortex bursting over the windward wing. This was demonstrated in the flow patterns corresponding to the centerline vertical tail configuration in Fig. 9. The decrease in the lift coefficient with sideslip is more gradual on the wing-mounted fin arrangement. The fins promote vortex bursting ahead of the wing trailing edge at $\beta = 0°$, whereas the chine and wing vortices are stable into the wake on the centerline tail configuration. As a consequence, the change in the vortex burst position due to sideslip is less pronounced on the former. In addition, sideslip will stabilize the vortex system on the leeward wing-fin combination, which will limit the lift loss associated with the advanced vortex breakdown on the windward side. The presence of the fins is manifested by the lower lift in comparison to the centerline tail configuration at sideslip angles to ±10°.

As maximum lift is approached, the sensitivity of the lift coefficient to the sideslip angle

increases, particularly on the configuration with the centerline vertical tail. At $\alpha = 25°$ (Fig. 21b), for example, the lift decreases abruptly as the sideslip angle is increased from 0° to ±10°. This trend is again the result of the windward chine-wing vortex breakdown. The flow patterns presented in Fig. 10 corresponding to the centerline tail configuration showed a stable chine-wing vortex system at $\beta = 0°$. At a sideslip angle of 5°, however, vortex bursting was predominant on the windward wing, and at $\beta = 10°$ breakdown had advanced to the chine-wing junction. The difference in the lift at $\beta = 0°$ between the centerline tail and outboard fin configurations is not apparent for $\beta \geq 5°$. At the higher angles of attack, sideslip reduces the influence of the fins on the vortex flow field and, hence, the lift since the vortex bursting has advanced upstream of the fin on the windward side and the chine-wing vortex flows are displaced away from the stabilizing surface on the leeward wing. The trends are the same at $\alpha = 30°$ (Fig. 21c).

At an angle of attack of 35° (Fig. 21d), the lift variation with sideslip is the same on the centerline tail and outboard fin configurations. The lift shows an initial slight increase with sideslip. This is attributed to the stabilization of the leeward vortices which had exhibited breakdown over the wing at $\beta = 0°$. This effect was illustrated in the vortex flow patterns in Fig. 12. A lift loss occurs with a further increase in the sideslip angle as a result of the continued forward traversal of the windward vortex bursting and the upward displacement of the leeward vortices from the wing surface.

Figure 22 compares the variation of the rolling-moment coefficient with the angle of attack at $\beta = 10°$ for the configurations with the centerline and wing-mounted tail surfaces. The data indicate that the rolling moment trends are not affected by the tail placement considered in the present investigation. The larger moment arm of the centerline tail promotes a nearly constant stable increment to C_ℓ at $\alpha = 0°$ to 10° in comparison to the wing-mounted fin arrangement. At angles of attack beyond 10°, however, the model with the outboard fins displays consistently higher values of the stable rolling-moment coefficient. In the present case, this is not due to a reduction in the vortex burst asymmetry in sideslip as reported in Ref. 5. Instead, the vortex-induced effects on the leeward wing surface are reduced as a result of the upward displacement of the chine forebody vortex because of the presence of the fin. This was discussed previously in conjunction with the flow-field sketches in Figs. 19 and 20. In addition, the contribution of the leeward fin to the stable rolling moment may be maintained to higher angles of attack owing to the postulated favorable flow field about the leeward wing. The rolling moment contribution of the centerline tail rapidly diminishes at angles

of attack greater than 20° as the windward-wing wake envelopes the vertical stabilizer.

Figure 23 compares the variation of the rolling moment coefficient with the sideslip angle at angles of attack from 20° to 35° corresponding to the centerline tail and wing-mounted fin configurations. At $\alpha = 20°$ (Fig. 23a), the variation of the rolling moment with sideslip is stable for both configurations at angles of sideslip generally from -5° to +10°. At β values outside this range, the centerline tail arrangement exhibits reduced roll stability/instability as a result of the tail stall. At $\alpha = 25°-35°$ (Figs. 23b-d), the model with the centerline tail typically exhibits a lateral sensitivity at small sideslip angles ($|\beta| \leq 5°$). The $\beta = 0°$ flow asymmetries that were discussed in connection with Fig. 6e contribute to the nonlinear rolling moment variations. In addition, the centerline tail configuration is susceptible to a pronounced upstream traversal of the windward chine-wing vortex system at small β values. In contrast, the wing-mounted fin configuration displays lateral stability within the same β range.

Figure 24 presents the yawing moment coefficient variations with the angle of attack at $\beta = 10°$. A comparison of the test data at $\alpha = 0°$ to 20° reveals more stable values of the yawing moment coefficient on the centerline vertical tail configuration. The centerline tail is exposed to a more favorable flow field relative to the wing-mounted fins since it is positioned in a region of higher dynamic pressure and is outside the region of influence of windward vortex bursting. At higher values of α, however, the model with the twin tails develops stable yawing moment increments relative to the centerline tail configuration. At angles of attack beyond 20°, the vortex-fin interaction on the leeward wing yields improved stabilizer effectiveness. In contrast, the low-energy wake from the windward wing blankets the centerline tail with a consequent decrease in its effectiveness.

The yawing moment variation with sideslip is shown in Fig. 25 corresponding to angles of attack from 20° to 35°. At $\alpha = 20°$ (Fig. 25a), the yaw stability is higher on the centerline tail model at sideslip angles from -5° to +10°. At sideslip angles outside this range, however, the latter configuration exhibits an unstable variation of C_n with α caused by the increased flow separation from the vertical tail. The twin-tail arrangement develops a higher level of yaw stability at $\alpha = 25°$ and sideslip angles to ±10° (Fig. 25b) owing to the beneficial influence of the leeward vortex system on the fin. At higher sideslip angles, both configurations display an unstable variation of the yawing moment with sideslip. This is due to the diminished tail effectiveness and the advancement of the chine vortex breakdown to a position over the forebody at the large sideslip angles. The yawing moment characteristics become increasingly nonlinear at higher

angles of attack. This is demonstrated in Figs. 25c and d corresponding to α = 30° and 35°, respectively. The twin-tail configuration continues to exhibit a more stable variation of the yawing moment with sideslip at sideslip angles from -5° to +5°. This is due to the combined contributions of the chine forebody and wing-mounted fins to the yaw stability as opposed to the isolated effect of the chine forebody on the centerline vertical tail configuration. At higher sideslip angles, the slope of the yawing moment curve becomes negative, indicating directional instability. This reflects the diminished influence of the leeward chine-wing vortex system on the fin and the reduced suction pressures on the windward forebody surface arising from the breakdown of the chine vortical flow.

Dynamic Roll Stability. Free-to-roll results for the chine-wing model with centerline tail revealed wing rock oscillations at angles of attack near maximum lift. This was a self-induced, small-amplitude lateral oscillation that may have been triggered by the vortex asymmetry noted previously and sustained by an unsteady chine-wing vortex breakdown phenomenon. Figure 26 presents a time history of the roll angle of the model.

Installation of the wing-mounted fins eliminated the wing rock as shown in the model roll angle time history in Fig. 27. The fins precluded the development of large flow asymmetries and the fore and aft traversal of the vortex breakdown positions, which were the speculated triggering and sustaining wing rock mechanisms, respectively, on the centerline tail configuration.

Effect of Chine Deflection

Forebody Upper Surface Static Pressures. Figures 28 and 29 show the effect of symmetric chine deflection angles of +45° (up) and -45° (down), respectively, on the forebody surface pressures at Stations 1 and 2 and angles of attack of 20°, 30°, and 40°. Station 1 is positioned just downstream of the modified nose region, while Station 2 is located farther aft at approximately 50% of the forebody length from the nose.

Upward deflection of the chine along the nose region promoted an increase in the forebody vortex-induced suction peaks and an inboard displacement of the suction pressure maxima at Station 1. This was indicative of a stronger vortex that was positioned farther inboard. The relatively unchanged pressure distributions at Station 2, however, indicate that the influence of the chine deflection was "damped out" farther aft on the forebody. Smoke flow visualizations showed that the vortex shed from the upwardly deflected chine was rapidly entrained into a dominant vortical flow generated along the undeflected portion of the chine forebody. This flow situation is depicted in the photograph in Fig. 30. The chine deflection, therefore, promoted only a local flow

disturbance, and there was sufficient length of the undeflected chine aft of the nose region for the vortical flow to reestablish itself. Similar effects were observed by Malcolm and Skow[6] in a water tunnel flow-visualization study of vortex flow control devices positioned near the apex of a wing leading-edge extension (LEX).

Downward deflection of the chine delayed the onset of vortex formation along the nose region to a higher angle of attack. Once the vortex had formed, however, the suction pressure peaks at Station 1 were higher and positioned farther outboard in comparison to the chine forebody with the unmodified nose. The flow-field changes associated with the chine deflection were again confined to the forward region of the forebody, however, as the vortex flow quickly reestablished itself along the undeflected length of the chine. This effect is evident in the pressure distributions at Station 2.

Longitudinal and Lateral-Directional Characteristics. The chine deflection had no effect on the longitudinal and lateral-directional characteristics as illustrated in Figs. 31-34 corresponding to the +45° (up) chine deployment. The results were similar for the -45° (downward) chine deflection and are not presented.

The force and moment results confirm that deflection of the chine along the nose region is an ineffective means of modulating the global flow field. This differs from the trends obtained on fighter configurations with "conventional" forebodies that lack a salient edge (a chine, for example) to fix the primary flow separation along their length. Numerous studies (Ref. 7, for example) have shown that small changes (minor surface imperfections, grit, and trip wires) to the nose region of forebody shapes representative of present-generation fighters can be amplified downstream to affect the entire 3-D flow field. On the chine forebody-slender wing combination, a more appropriate location for passive/active flow modulators may be at or near the chine-wing juncture to affect the vortex interaction and breakdown phenomena at the high angles of attack.

Summary

An exploratory test was conducted in the NASA Langley Research Center's 12-Foot Low-Speed Wind Tunnel of the nonlinear aerodynamic and stability characteristics of a generic fighter configuration featuring a chine-shape forebody and 60° cropped delta wing. Emphasis was placed on the improved understanding of highly interactive forebody and wing vortex flows at extreme attitudes (angles of attack and sideslip) and the correlation of the vortex flow behavior with the configuration forces and moments. To aid in quantifying the effects of a coupled forebody-wing vortex system, the 60° cropped delta wing model was tested with a tangent-ogive forebody to provide data on

uncoupled forebody-wing vortices. A comparative study was made of vortex-empennage interactions by testing the chine forebody-cropped delta wing configuration with centerline vertical tail and wing-mounted fins. The "wing rock" behavior of these configurations was evaluated. Modifications were made to the chine forebody that featured symmetric deflections of the chine along the nose region. The effects of the forebody modifications on the configuration flow field and aerodynamic and stability characteristics were assessed.

The test results showed that the concentrated vortices generated by the chine forebody and cropped delta wing interacted favorably to promote large nonlinear lift increments at moderate-to-high angles of attack. A concurrent effect was increased pitch instability because of the forebody vortex lift acting far ahead of the center of gravity. This effect was particularly severe at post-stall angles of attack. The forebody vortex interaction with the wing flow field delayed complete stall of the windward wing. Consequently, the lateral aerodynamic characteristics were improved. The chine forebody was effective in developing and sustaining a concentrated vortex along its windward side up to high attitudes, and this vortical flow induced large restoring yawing moments. The chine-wing vortex system was susceptible to severe asymmetries in the core breakdown positions in sideslip. As a result, the forebody-wing vortex interaction did not alleviate the lateral sensitivity near maximum lift. In addition, the coupled vortex system exhibited significant hysteresis. The bursting of the windward chine vortex over the forebody at high angles of attack led to large, unstable yawing moments.

The advanced breakdown of the chine and wing vortices due to the wing-mounted fins caused a large lift loss at angles of attack up to stall and a corresponding increase in the pitch instability in comparison to the configuration with centerline vertical tail. The fins improved the lateral-directional characteristics at high angles of attack. The beneficial effect in roll was associated with the diminished influence of the chine-wing vortices on the leeward wing arising from an upward displacement of the vortical flows. The leeward fin was positioned in a more favorable flow field relative to the centerline tail, which was responsible for the beneficial effect in yaw. In general, the chine forebody-slender wing configuration with outboard fins exhibited less severe lift loss and more stable, linear variations of the rolling moment and yawing moment with sideslip near maximum lift. In addition, the fins eliminated the lateral oscillations

(wing rock) developed by the model with centerline vertical tail.

Deflection of the chines along the nose region caused only local flow-field changes and had no effect on the longitudinal and lateral-directional characteristics. The forebody pressure distributions and flow-field observations indicated that there was sufficient forebody area downstream of the modified nose region for the vortex flow to reestablish itself. The off-body flow visualization and force and moment measurements provided a basis for future studies aimed at the control of the forebody and wing vortical motions. Specifically, passive and/or active flow effectors positioned in the region of the chine-wing junction, where the vortex core interaction and breakdown occur near maximum lift, may yield improved aerodynamic, stability, and control characteristics at extreme attitudes.

References

[1]Erickson, G. E. and Brandon, J. M., "Low-Speed Experimental Study of the Vortex Flow Effects of a Fighter Forebody Having Unconventional Cross-Section," AIAA Paper 85-1798-CP, Aug. 1985.

[2]Skow, A. M. and Erickson, G. E., "Modern Fighter Aircraft Design for High-Angle-of-Attack Maneuvering," AGARD Lecture Series 121 presented at NASA Langley Research Center, March 1982.

[3]Hall, R. M., "Influence of Forebody Cross-Sectional Shape on Wing Vortex Burst Location," AIAA Paper 86-1835, June 1986.

[4]Wentz, W. H., Jr. and Kohlman, D. L., "Wind Tunnel Investigations of Vortex Breakdown on Slender Sharp-Edge Wings," NASA CR 98737, Nov. 1968.

[5]Johnson, J. L., Jr., Grafton, S. B., and Yip, L. P., "Exploratory Investigation of the Effects of Vortex Bursting on the High Angle-of-Attack Lateral-Directional Stability Characteristics," AIAA Paper 80-0463, 1980.

[6]Malcolm, G. N. and Skow, A. M., "Improved High Angle of Attack Controllability Through Vortex Manipulation," AFWAL-TR-86-101, Jan. 1986.

[7]Erickson, G. E. and Gilbert, W. P., "Experimental Investigation of Forebody and Wing Leading-Edge Vortex Interactions at High Angles of Attack," AGARD-CP-342, July 1983.

Table 1 Wing geometry
details

AR	1.73
b	3.90 ft
c_r	3.94 ft
c_t	0.56 ft
$\bar{c}$	2.67 ft
S_{ref}	8.78 ft^2
Λ_{LE}	60°
λ	0.14

Wing section - flat plate
(0.75-in.
thickness)
All wing edges sharp with
symmetrical bevel

STATION

21.60

HEMISPHERICAL CAP

3.60

45°

10.31

VERTICAL FINS

4.99

45°

15.27

73.40

27.35 23.00

60°

5.50

(a)

(b)

(c)

(d)
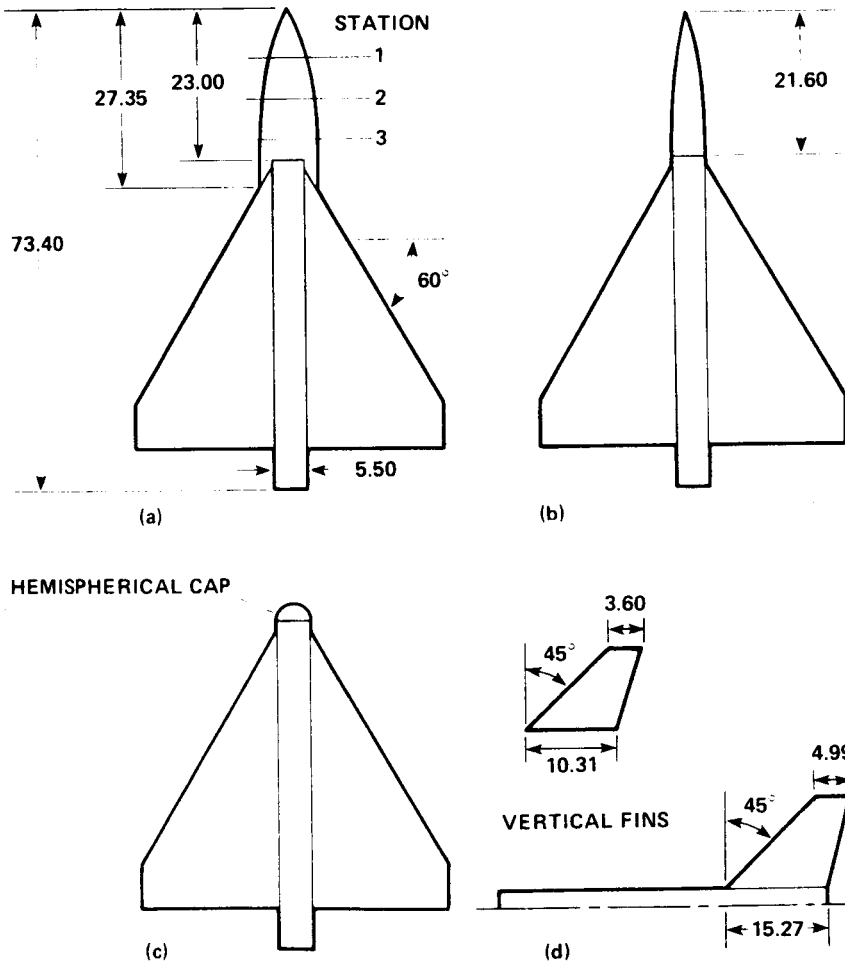
ALL DIMENSIONS ARE IN INCHES

Fig. 1 Details of the generic fighter wind tunnel model (in.). a) Blended forebody and
strake; b) ogive forebody; c) forebody removed; d) centerline vertical tail.

STATION 2
STATION 1   STATION 3

d = 8.70

ℓ = 27.35

(a)

STATION 2   STATION 3
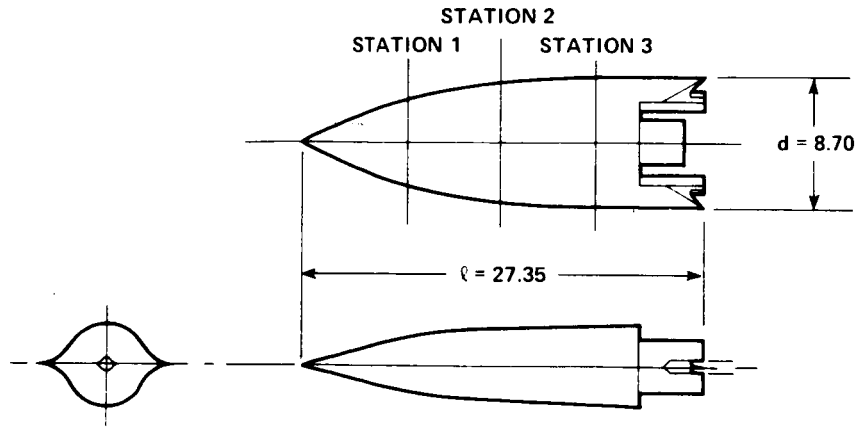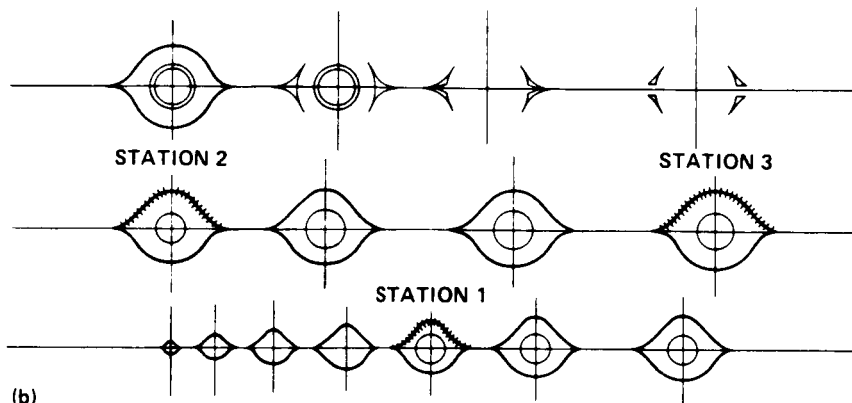
STATION 1

(b)

ALL DIMENSIONS ARE IN INCHES

Fig. 2 Details of the blended forebody and strake geometry and upper-surface static-pressure orifice locations (in.). a) forebody three-view; b) forebody cross sections.

21 0.04 O.D. PRESSURE TUBES EQUALLY SPACED ON UPPER SURFACE

Y

S (BODY)

FS 7.19

25 0.04 O.D. PRESSURE TUBES EQUALLY SPACED ON UPPER SURFACE

Y

S (BODY)

FS 13.56

STATION

1

2

3

29 0.04 O.D. PRESSURE TUBES EQUALLY SPACED ON UPPER SURFACE

Y

S (BODY)

FS 19.94

(c)
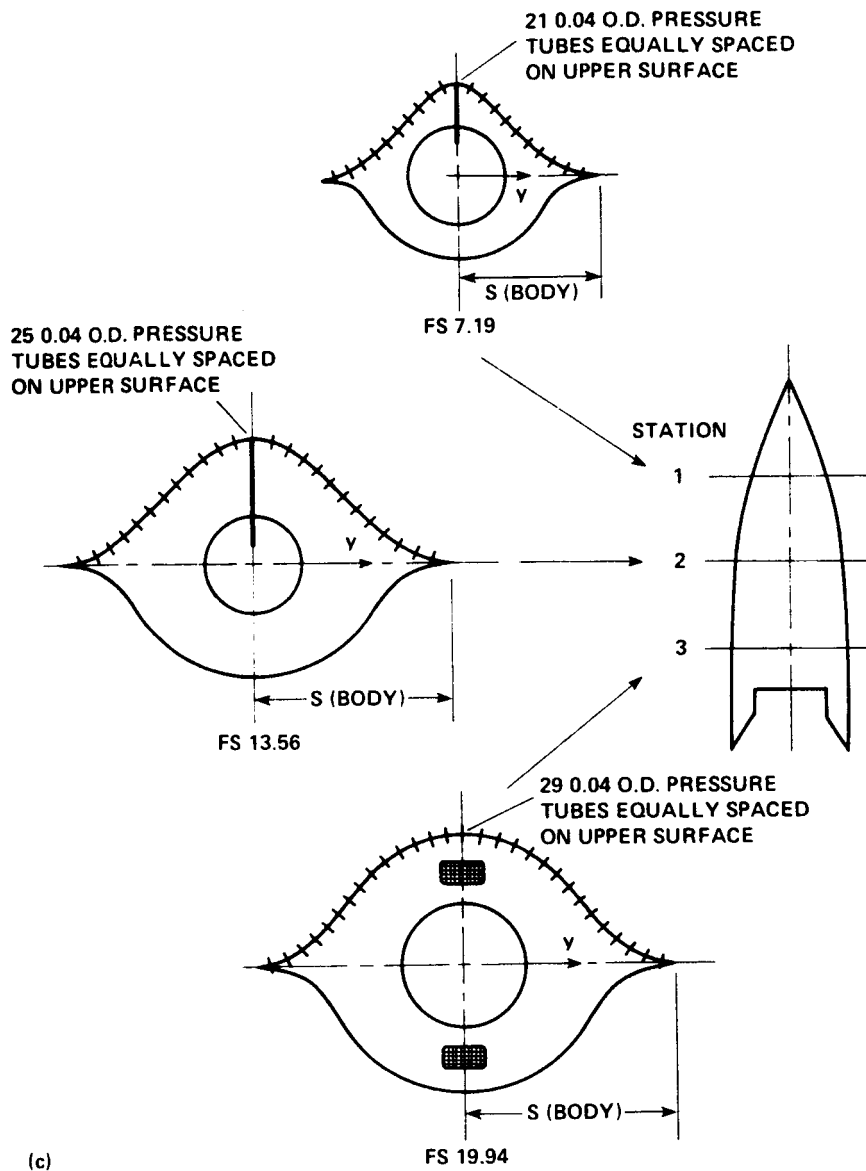
Fig. 2 Concluded. c) forebody upper-surface static-pressure orifice locations.
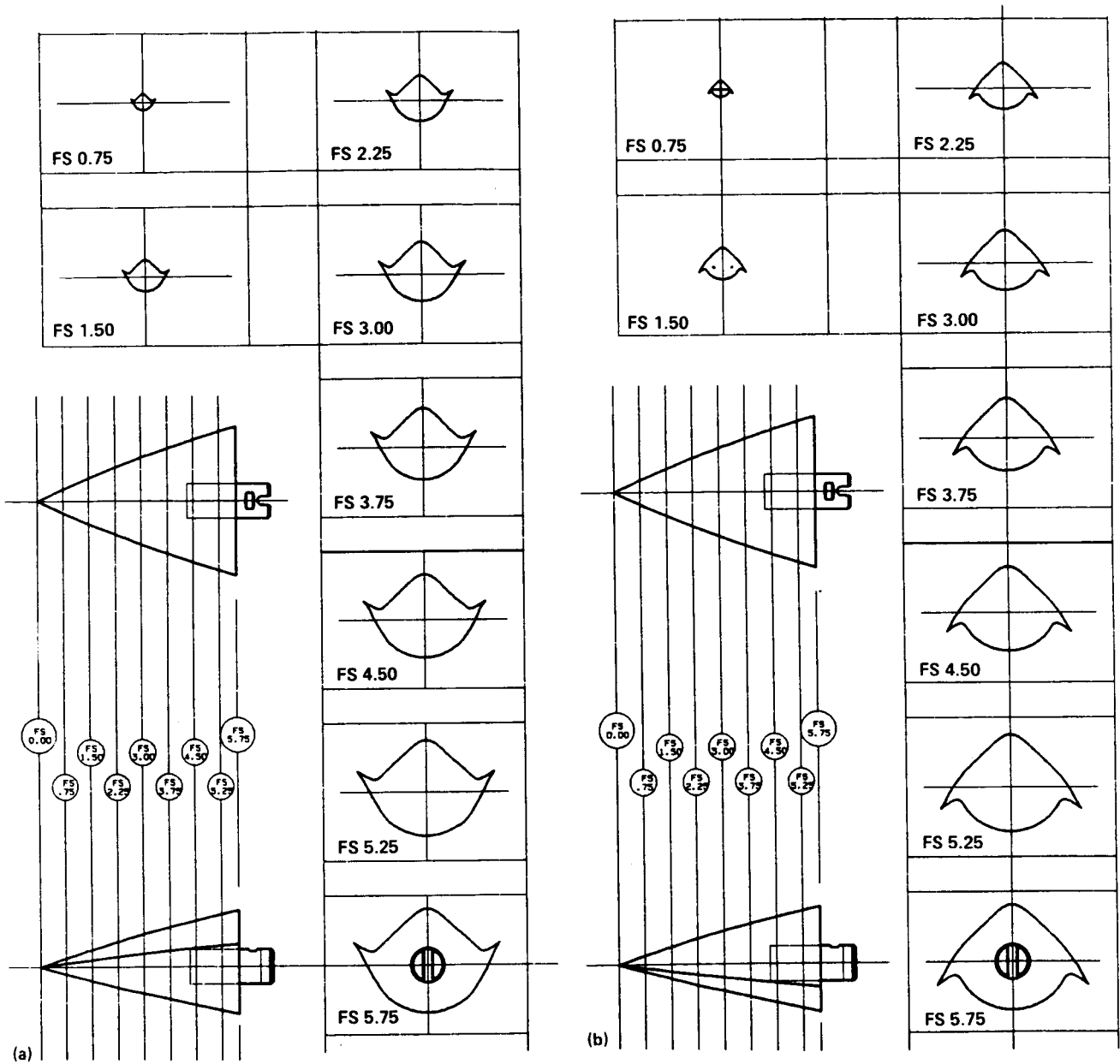
Fig. 3 Deflected chine components. a) 45° up; b) 45° down.

Fig. 4 Photographs of the chine forebody model installed in the NASA Langley 12-Foot Low-Speed Wind Tunnel.

16
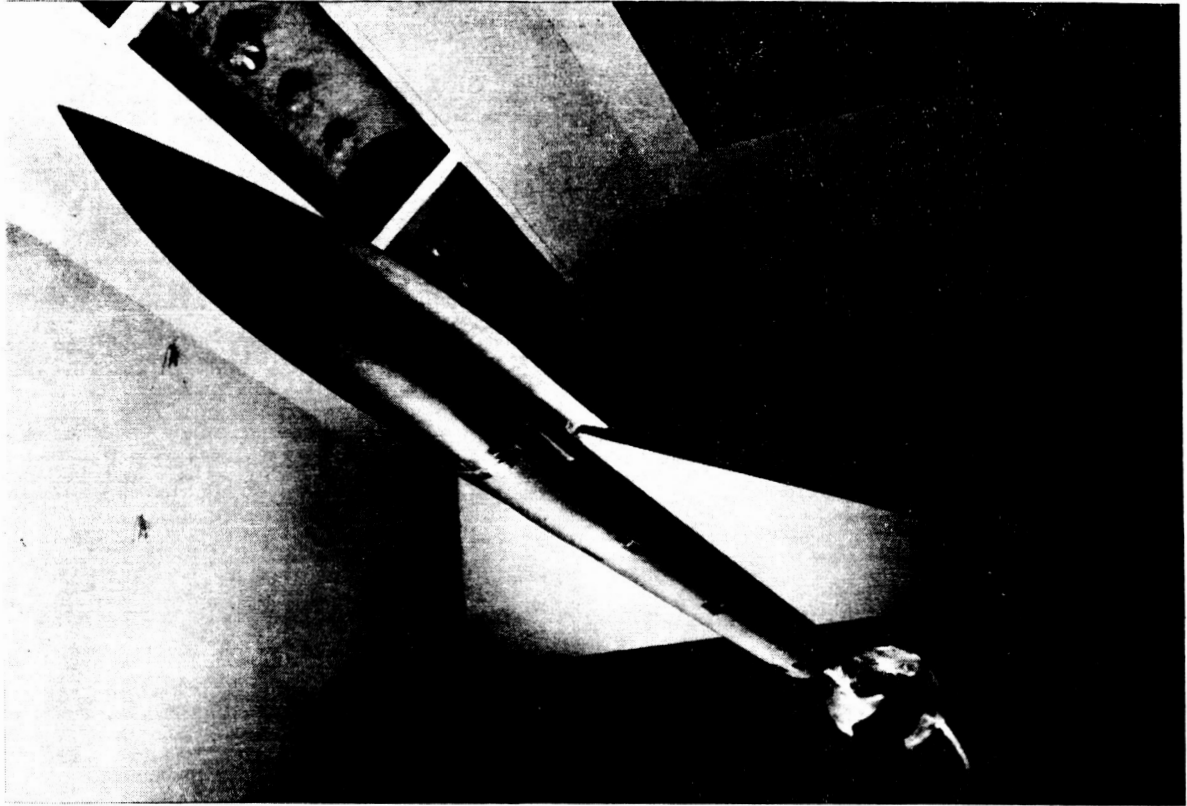
Fig. 4 Concluded.
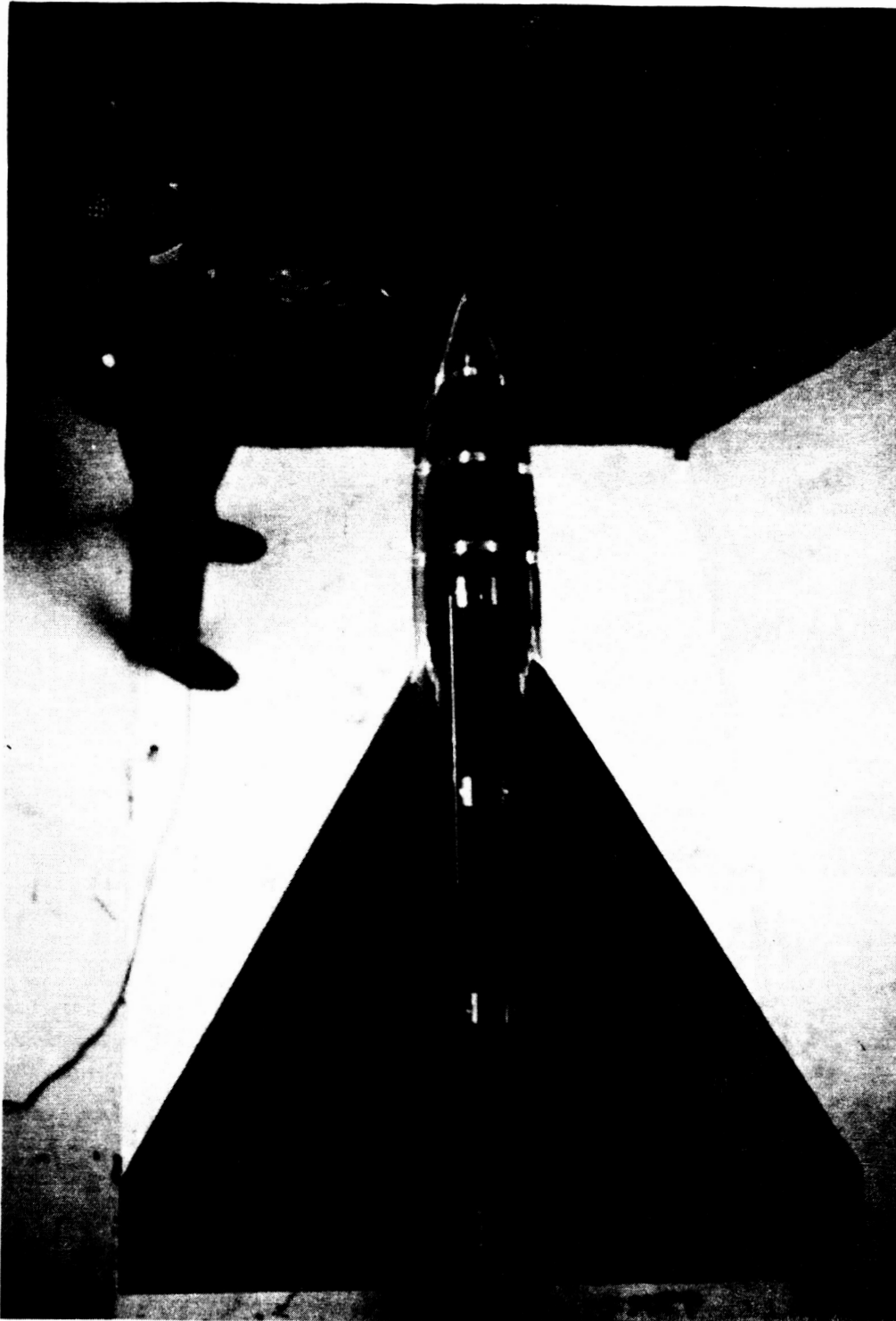
Fig. 5 Smoke flow visualization of chine forebody vortex interaction with the wing flow field; $\alpha = 25°$.

CHINE FOREBODY   TANGENT-OGIVE
                    FOREBODY

CHINE FOREBODY   TANGENT-OGIVE
                    FOREBODY

(a)

(b)

(c)

(d)
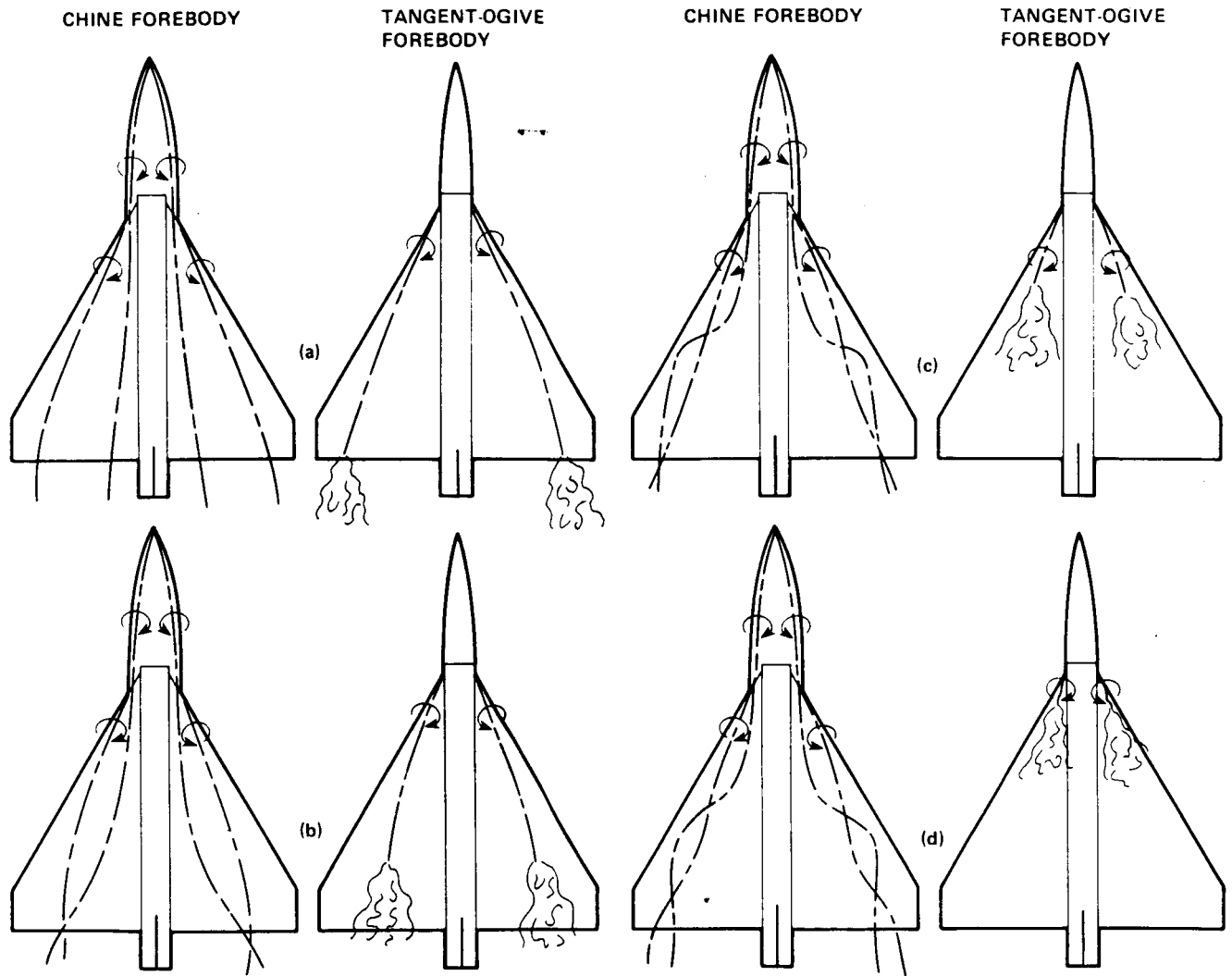
Fig. 6 Vortex flow patterns on the chine and tangent-ogive forebody configurations;
β = 0°. a) α = 10°; b) α = 15°; c) α = 20°; d) α = 25°.

CHINE FOREBODY

TANGENT-OGIVE
FOREBODY

(e)

CHINE FOREBODY

TANGENT-OGIVE
FOREBODY

(f)

(g)
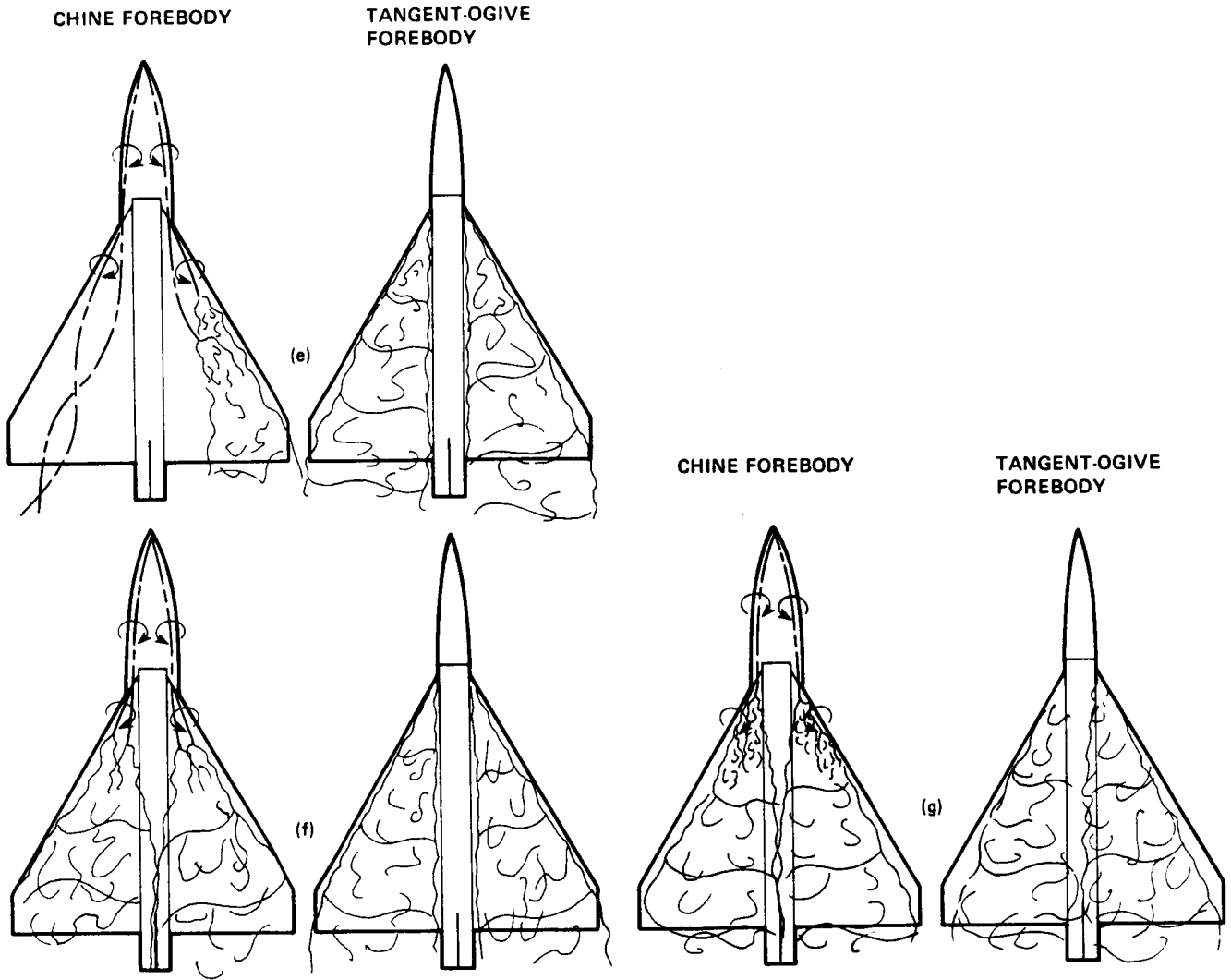
Fig. 6 Concluded.   e) $\alpha = 30°$; f) $\alpha = 35°$; g) $\alpha = 40°$.
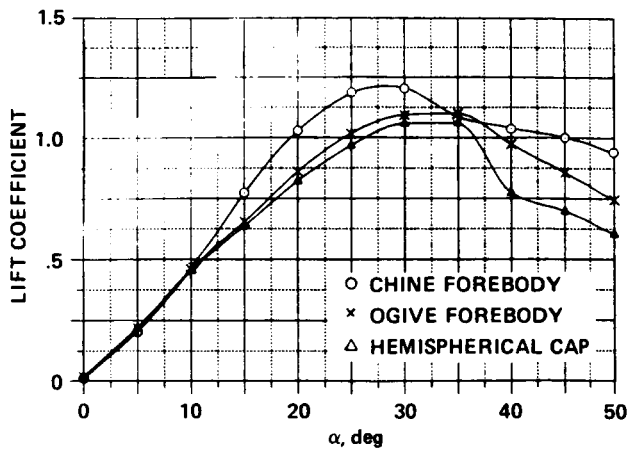
Fig. 7 Comparison of the lift characteristics of the chine, tangent-ogive, and hemispherical-cap forebody configurations.
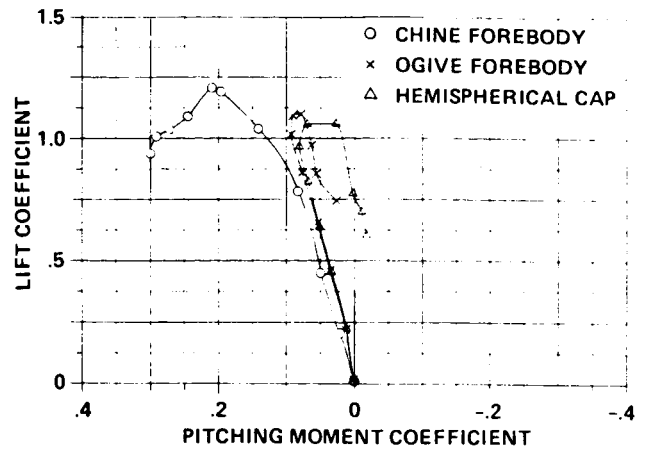
Fig. 8 Comparison of the pitching-moment characteristics of the chine, tangent-ogive, and hemispherical-cap forebody configurations.
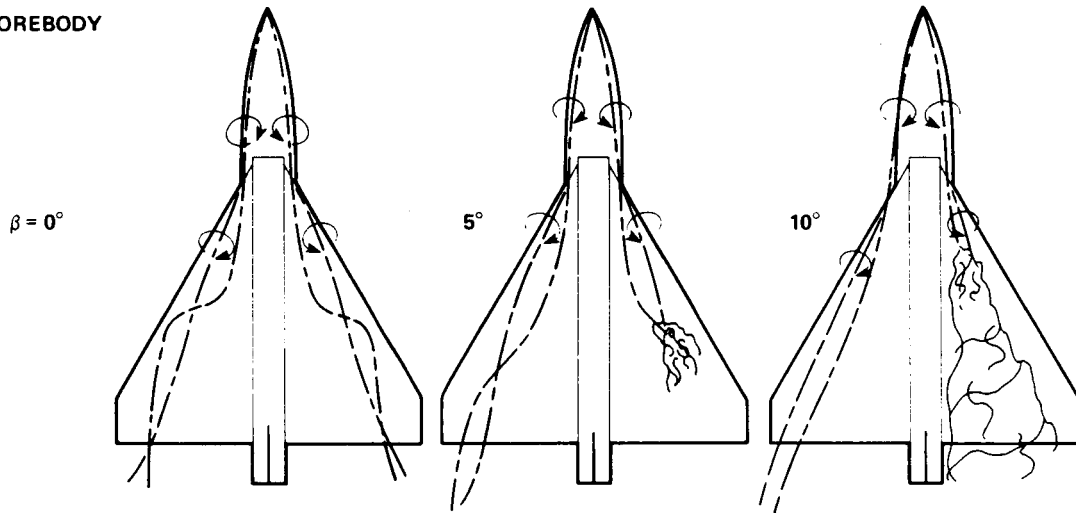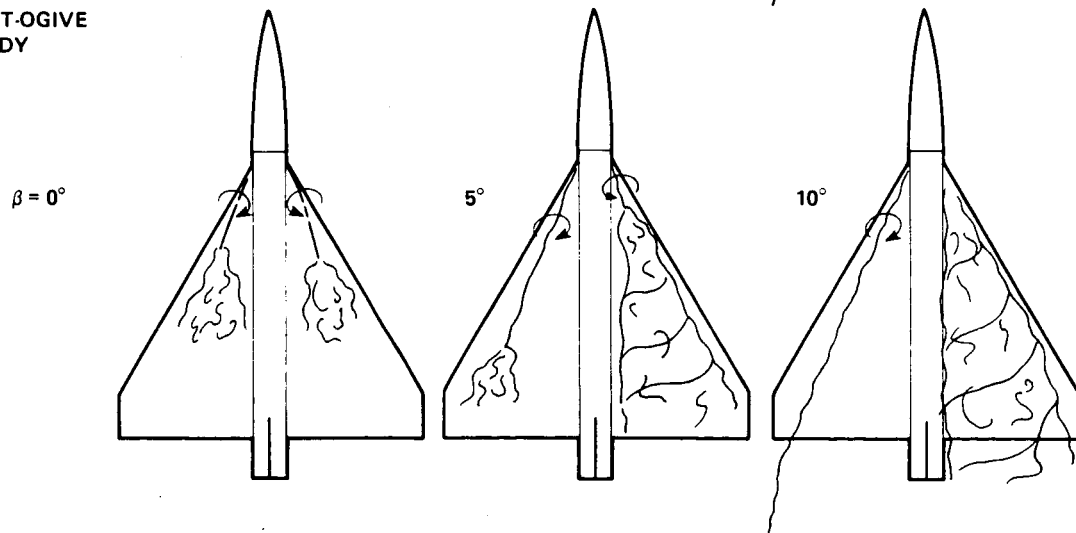
Fig. 9 Vortex flow patterns at α = 20°.

CHINE FOREBODY

$\beta = 0°$ 5°   10°

TANGENT-OGIVE
FOREBODY

$\beta = 0°$ 5°   10°
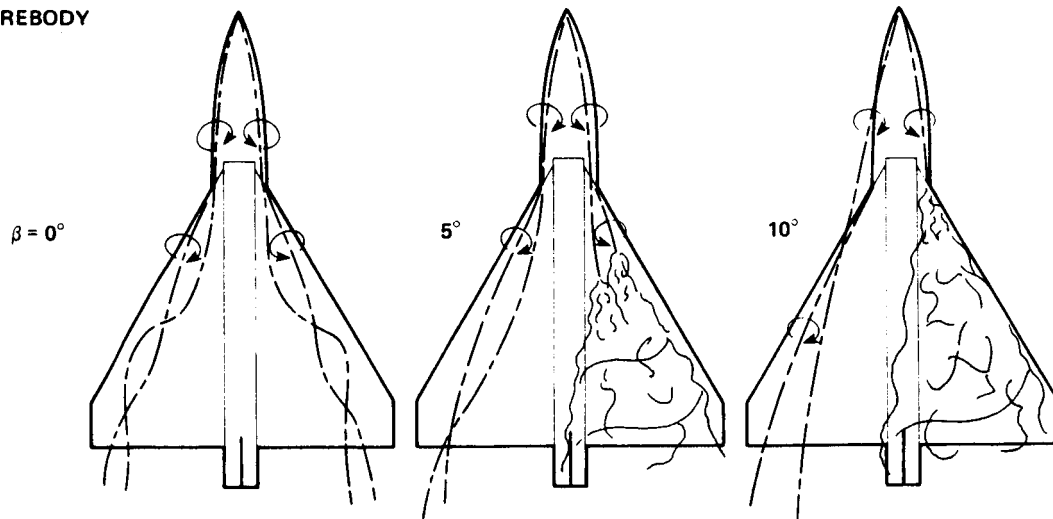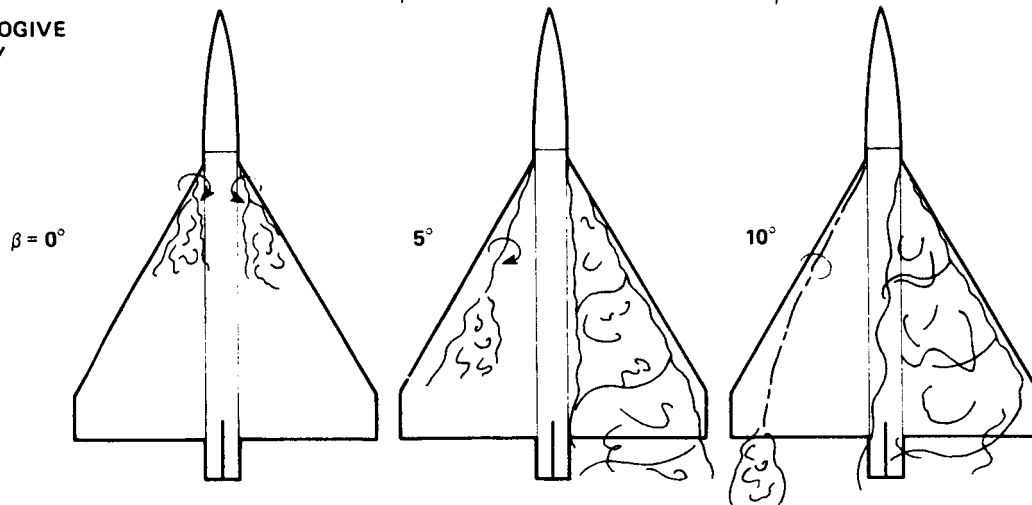
Fig. 10   Vortex flow patterns at $\alpha = 25°$.

CHINE
FOREBODY

$\beta = 0°$ 5°   10°

TANGENT-OGIVE
FOREBODY

$\beta = 0°$ 5°   10°
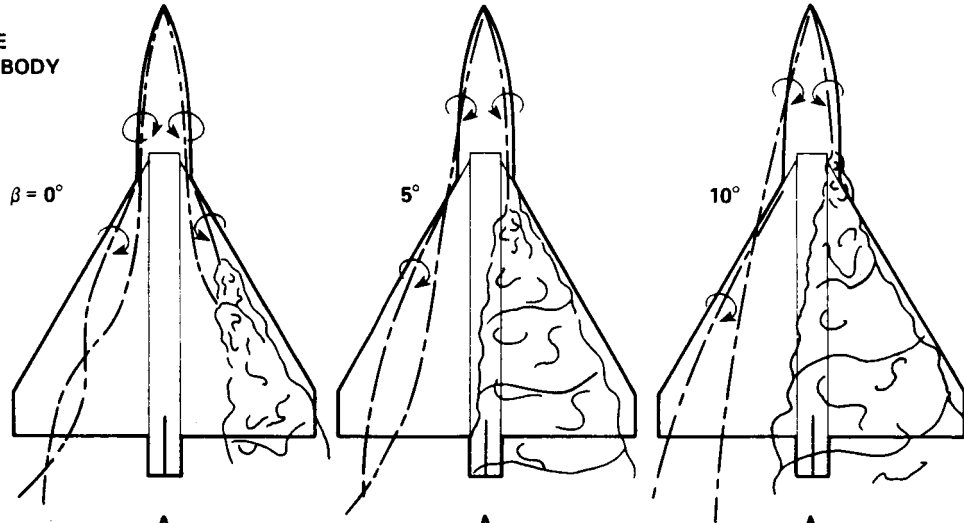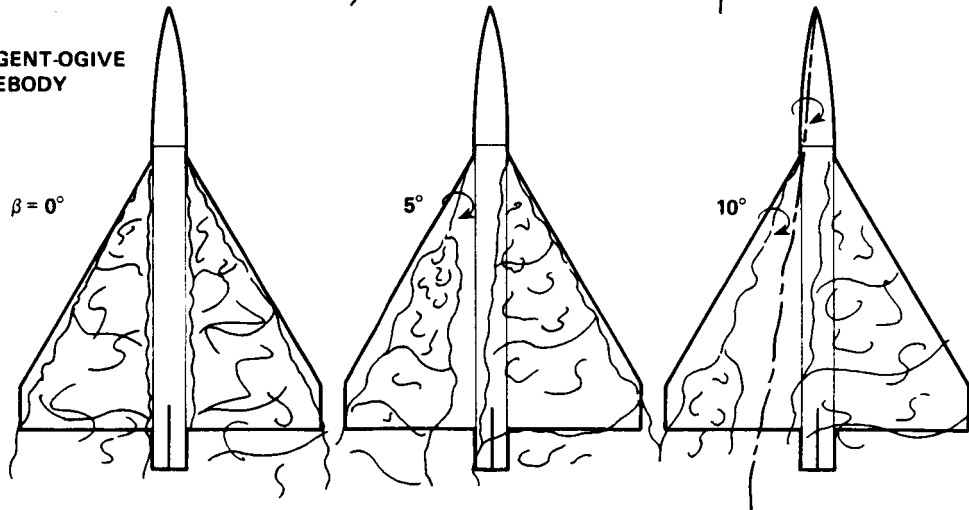
Fig. 11   Vortex flow patterns at $\alpha = 30°$.

CHINE FOREBODY

$\beta = 0°$ 5°   10°
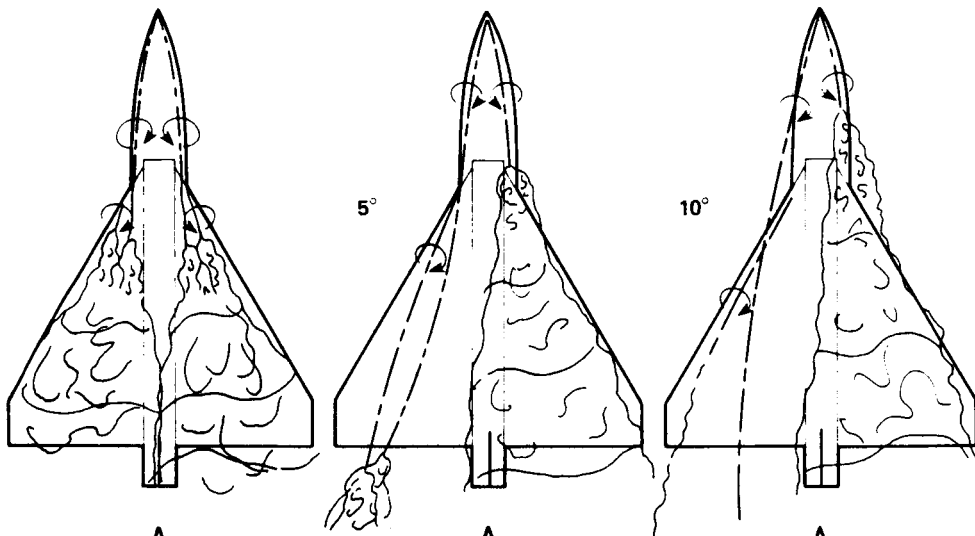
TANGENT-OGIVE FOREBODY

$\beta = 0°$ 5°   10°
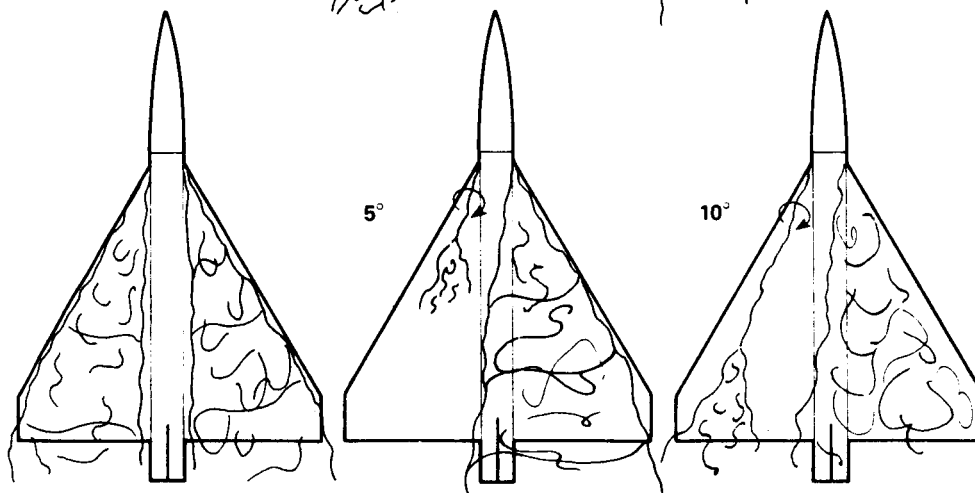
Fig. 12   Vortex flow patterns at $\alpha = 35°$.
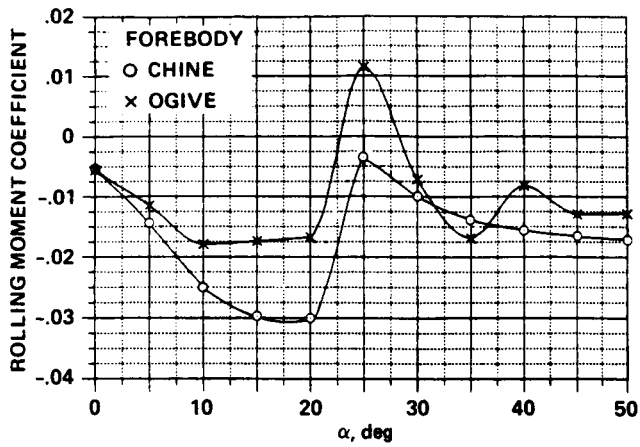
Fig. 13 Comparison of the rolling-moment characteristics of the chine and tangent-ogive forebody configurations at β = 10°.
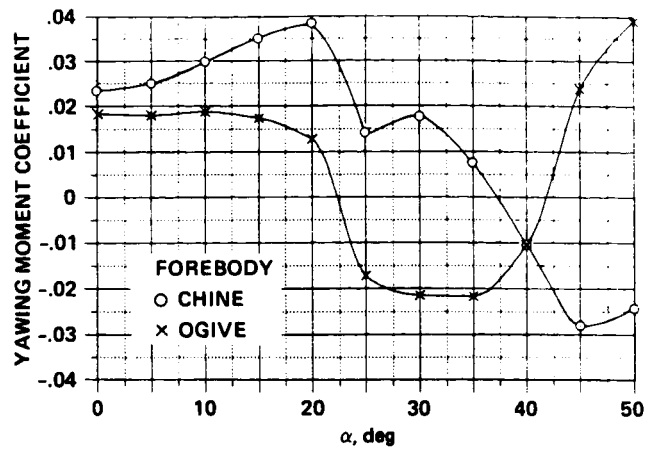
Fig. 14 Comparison of the yawing-moment characteristics of the chine and tangent-ogive forebody configurations at β = 10°.
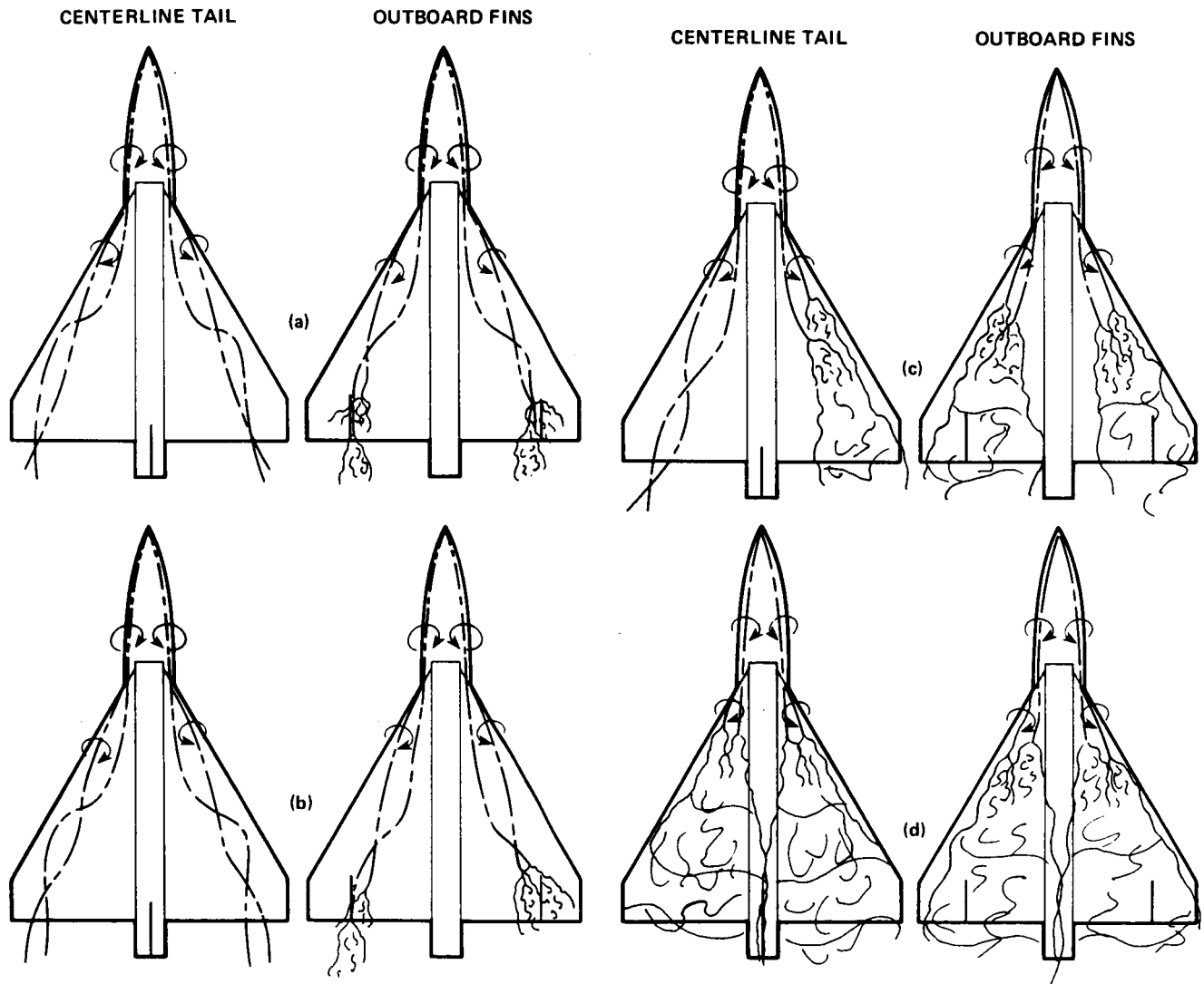
Fig. 15 Vortex flow patterns on the chine forebody model with centerline vertical tail and wing-mounted fins; β = 0°. a) α = 20°; b) α = 25°; c) α = 30°; d) α = 35°.

25
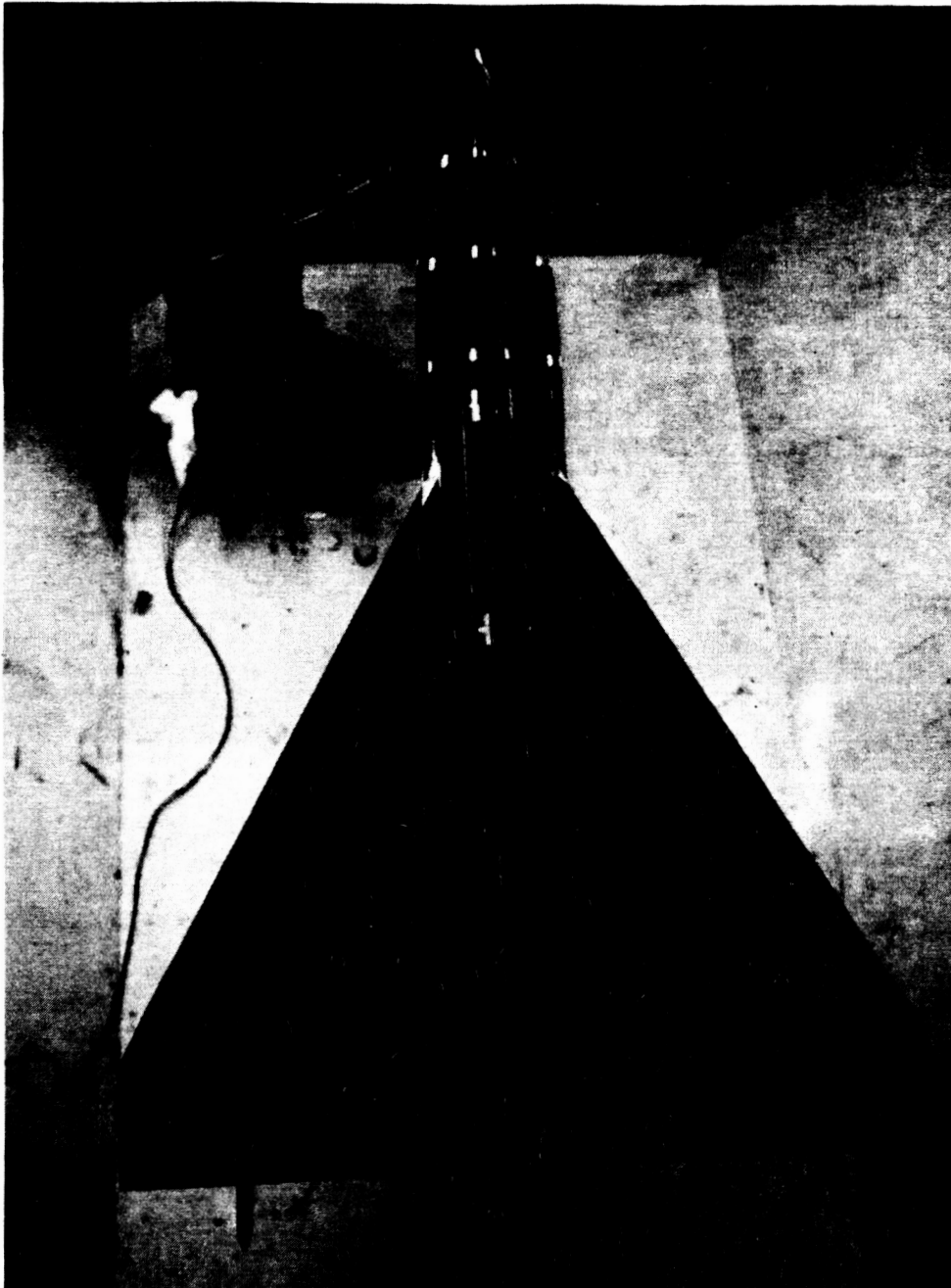
Fig. 16   Smoke flow visualization of chine forebody vortex bursting at outboard-mounted fin;
$\alpha = 25°$.
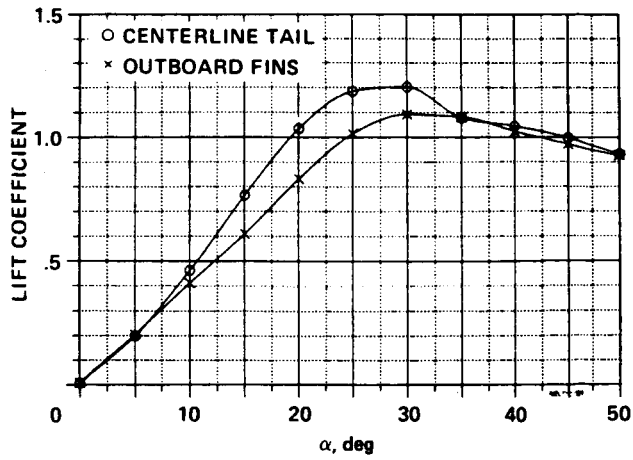
Fig. 17 Comparison of the lift characteristics of the chine forebody model with centerline vertical tail and wing-mounted fins.
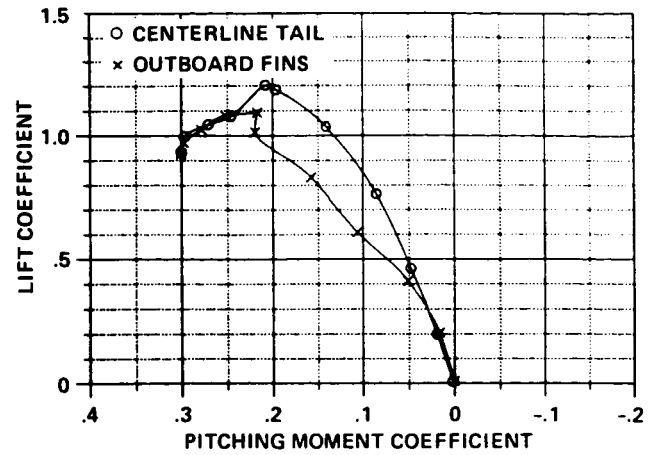
Fig. 18 Comparison of the pitching-moment characteristics of the chine forebody model with centerline vertical tail and wing-mounted fins.

CENTERLINE TAIL
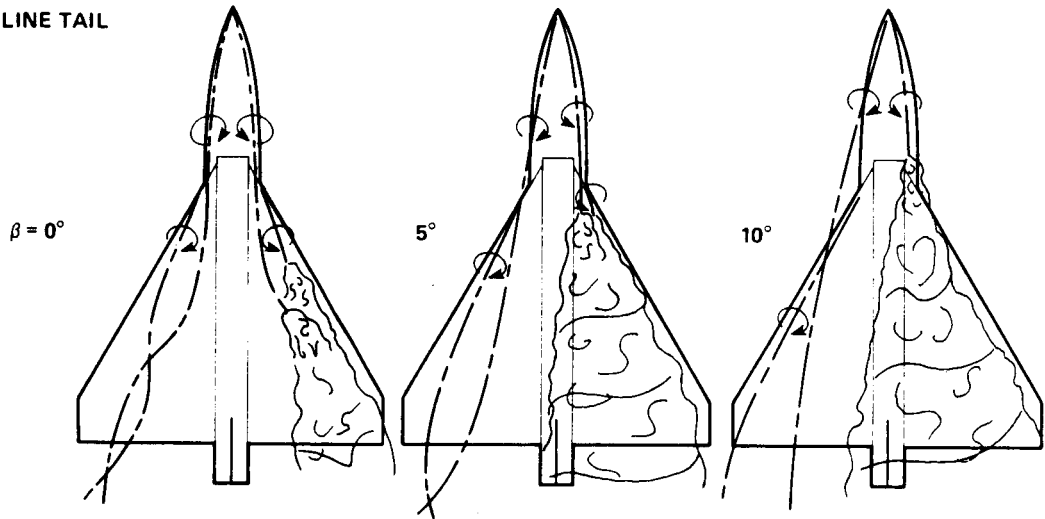
OUTBOARD FINS
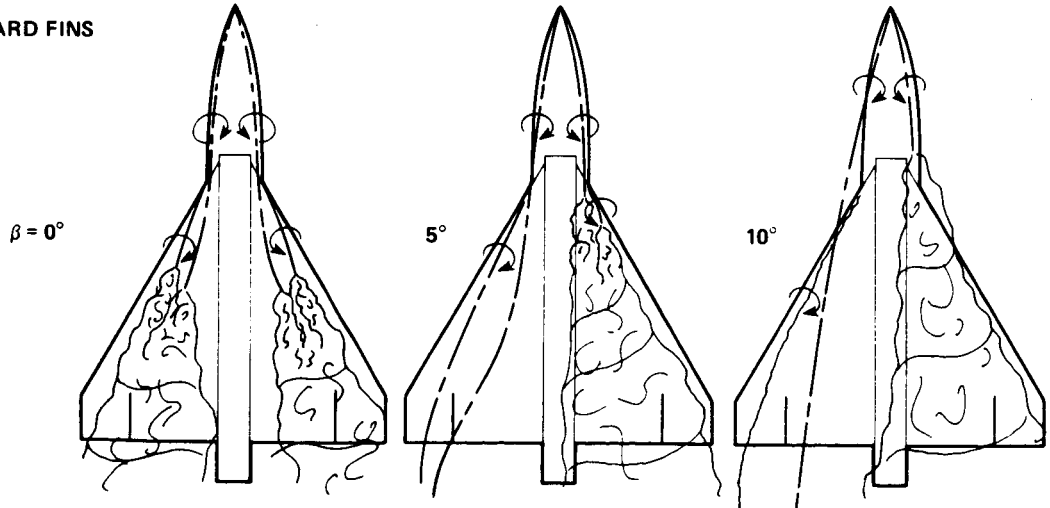
Fig. 19 Vortex flow patterns at α = 30°.

27

CENTERLINE TAIL

$\beta = 0°$ 5°   10°
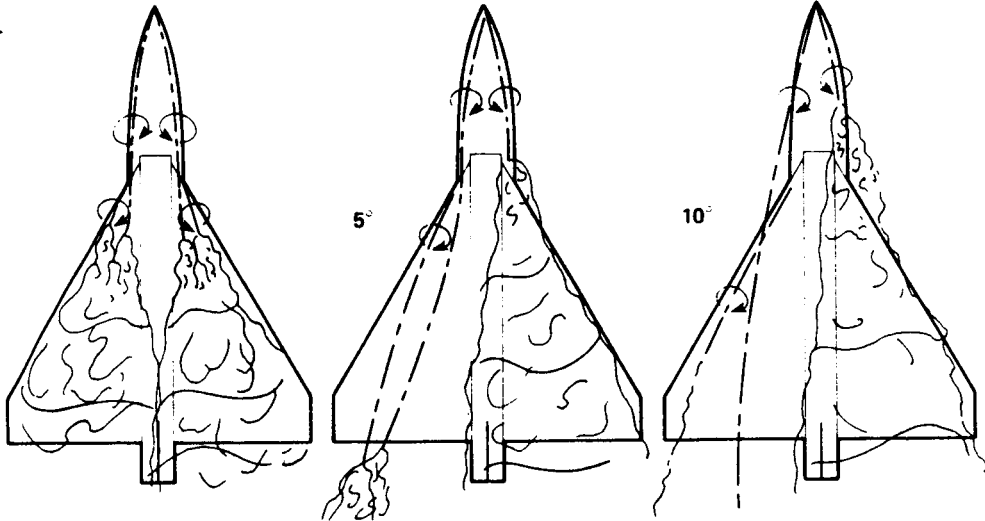
OUTBOARD FINS

$\beta = 0°$ 5°   10°
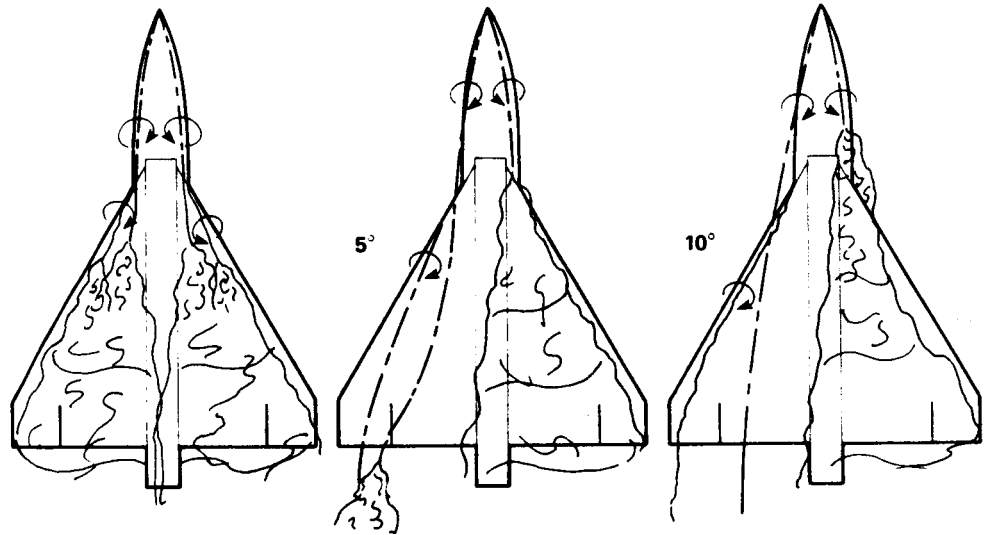
Fig. 20 Vortex flow patterns at $\alpha = 35°$.
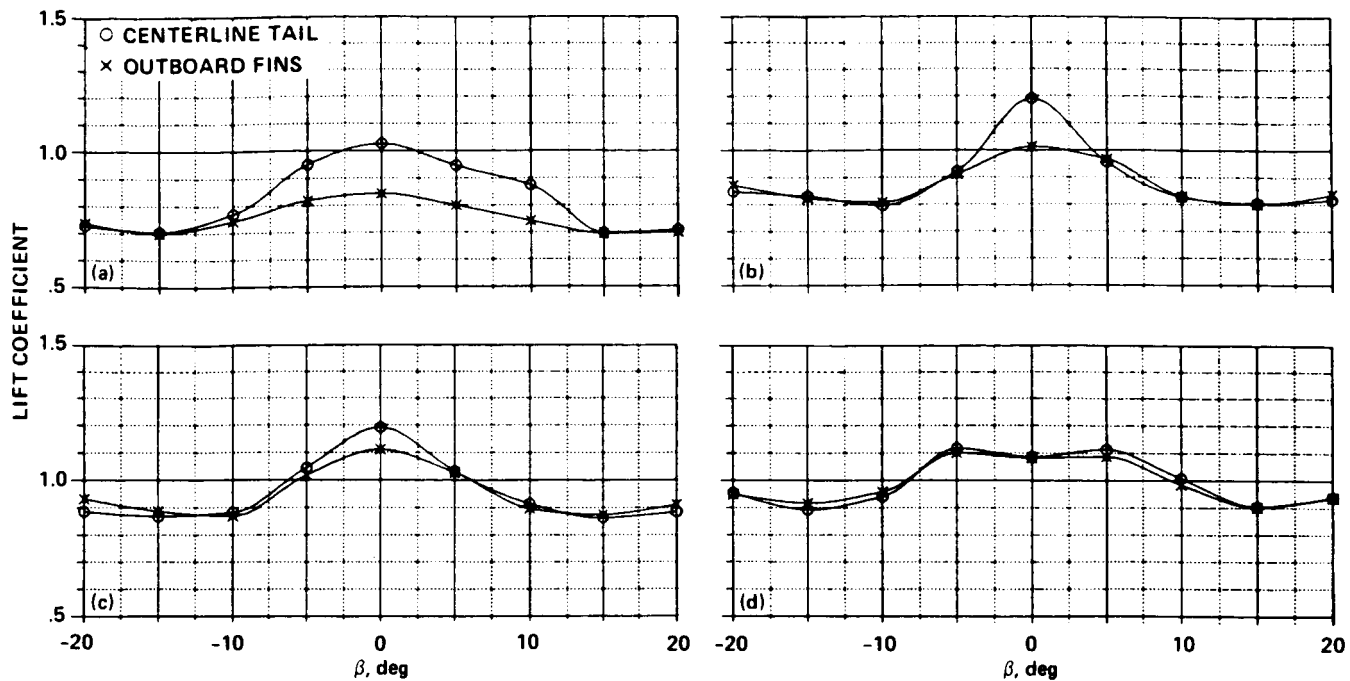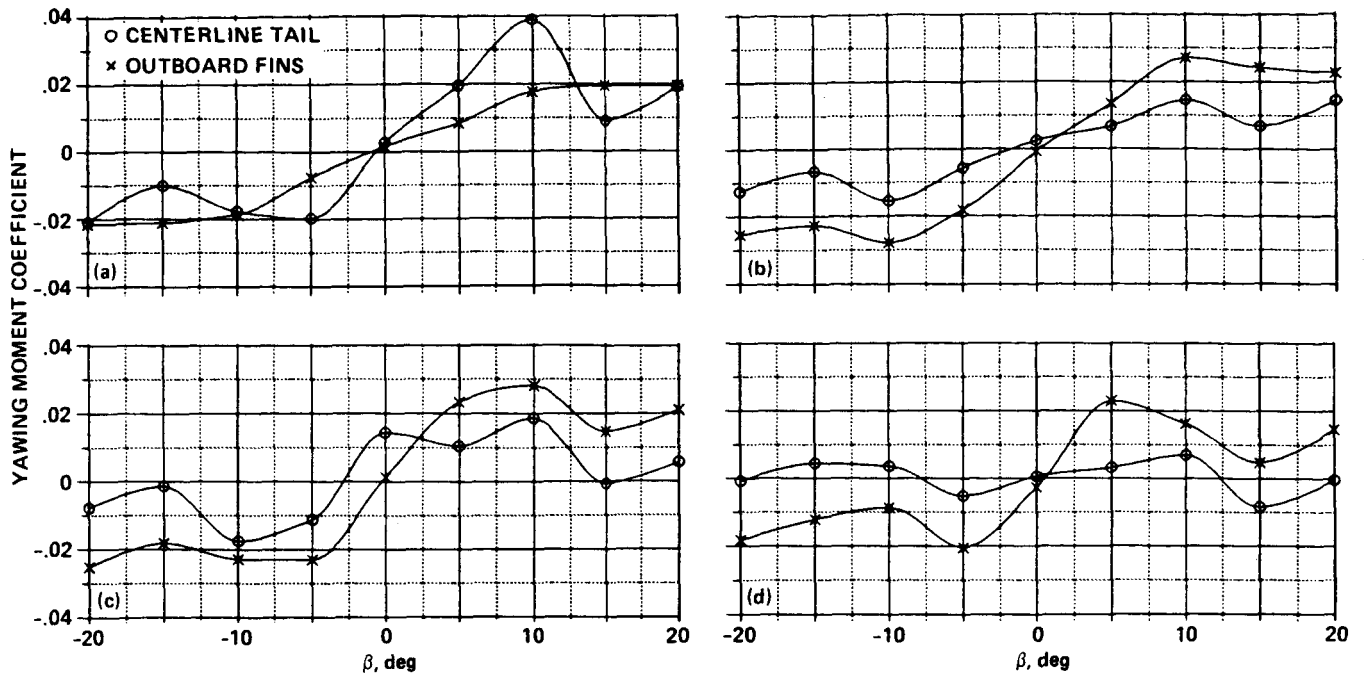
Fig. 21 Comparison of the lift variation with sideslip on the chine forebody model with centerline tail and outboard fins. a) α = 20°; b) α = 25°; c) α = 30°; d) α = 35°.
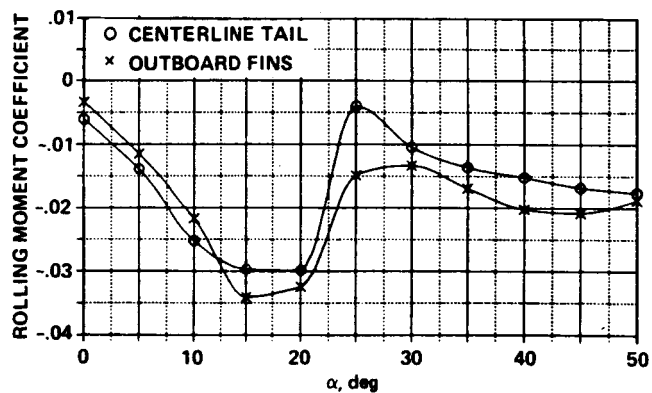
Fig. 22 Comparison of the rolling-moment characteristics of the chine forebody model with centerline tail and outboard fins; β = 10°.

Fig. 23 Comparison of the rolling-moment variation with sideslip on the chine forebody model with centerline tail and outboard fins. a) $\alpha = 20°$; b) $\alpha = 25°$; c) $\alpha = 30°$; d) $\alpha = 35°$.
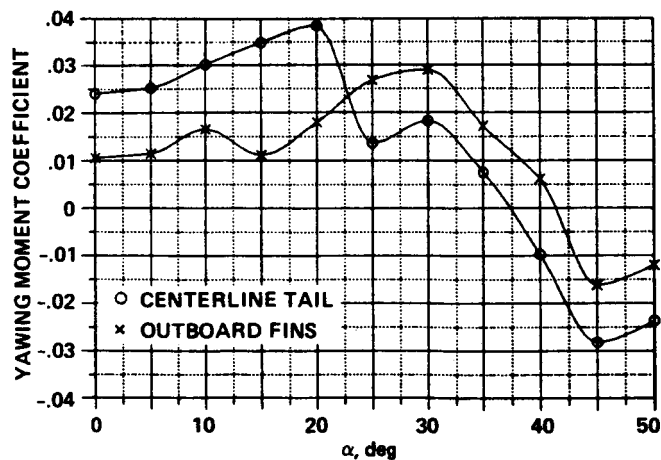
Fig. 24 Comparison of the yawing-moment characteristics of the chine forebody model with centerline tail and outboard fins; $\beta = 10°$.

Fig. 25 Comparison of the yawing-moment variation with sideslip on the chine forebody model with centerline tail and outboard fins. a) $\alpha = 20°$; b) $\alpha = 25°$; c) $\alpha = 30°$; d) $\alpha = 40°$.
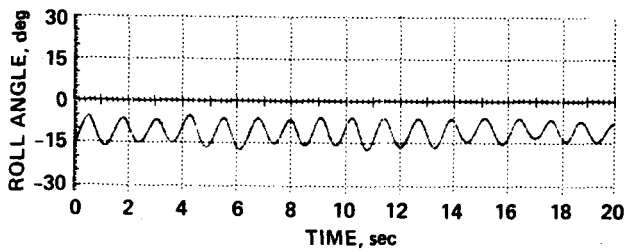
Fig. 26 Time history of the roll angle of the chine forebody model with centerline tail; $\alpha = 30°$.
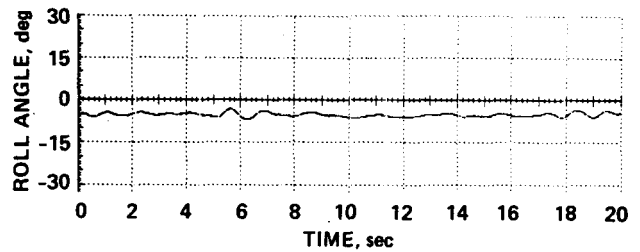
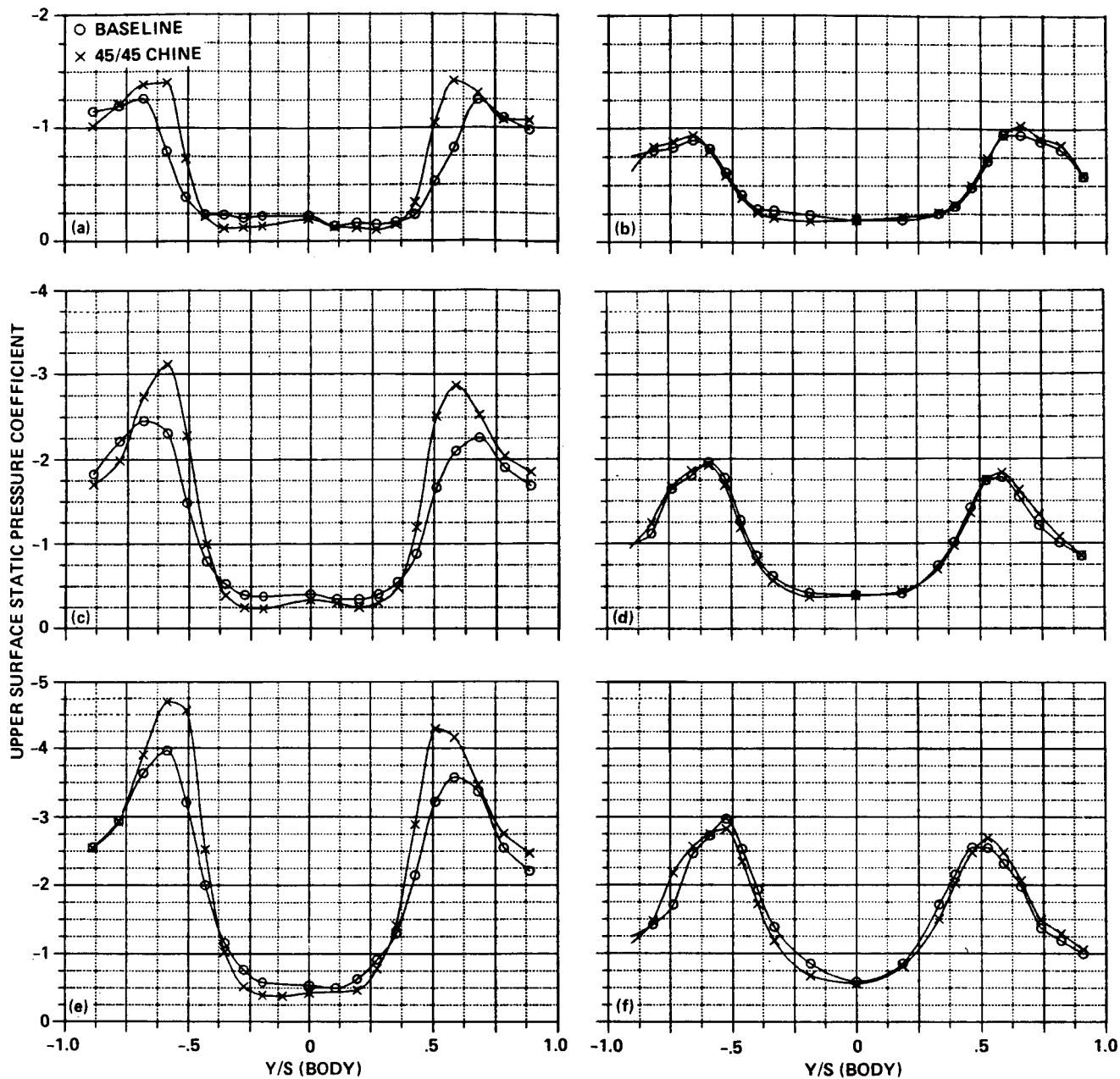Fig. 27 Time history of the roll angle of the chine forebody model with outboard fins; $\alpha = 30°$.

Fig. 28 Effect of 45° (upward) chine deflection on the forebody upper-surface static-pressure distributions. a) α = 20°, Station 1; b) α = 20°, Station 2; c) α = 30°, Station 1; d) α = 30°, Station 2; e) α = 40°, Station 1; f) α = 40°, Station 2.
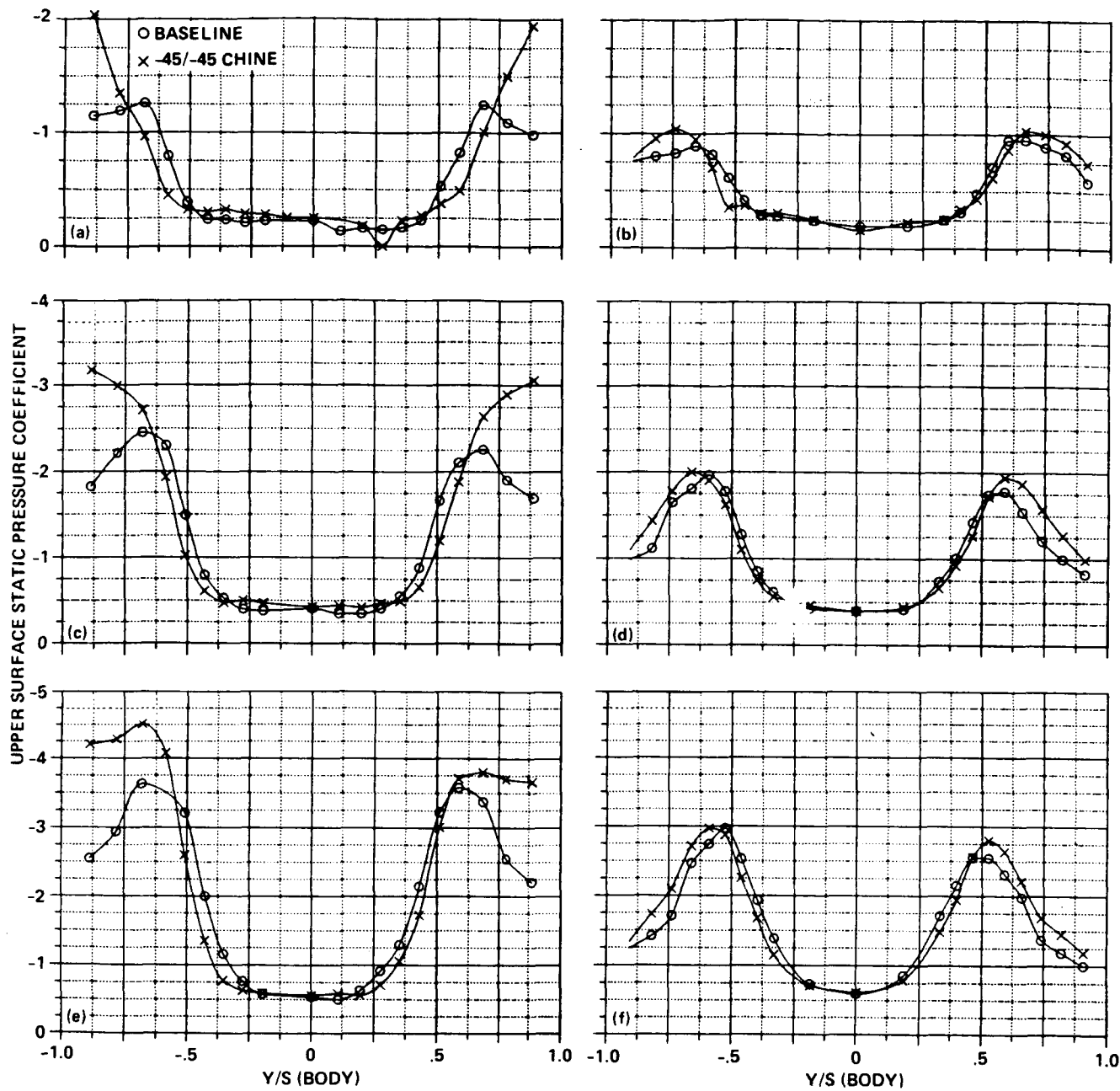
Fig. 29 Effect of -45° (downward) chine deflection on the forebody upper-surface static-pressure distributions. a) α = 20°, Station 1; b) α = 20°, Station 2; c) α = 30°, Station 1; d) α = 30°, Station 2; e) α = 40°, Station 1; f) α = 40°, Station 2.
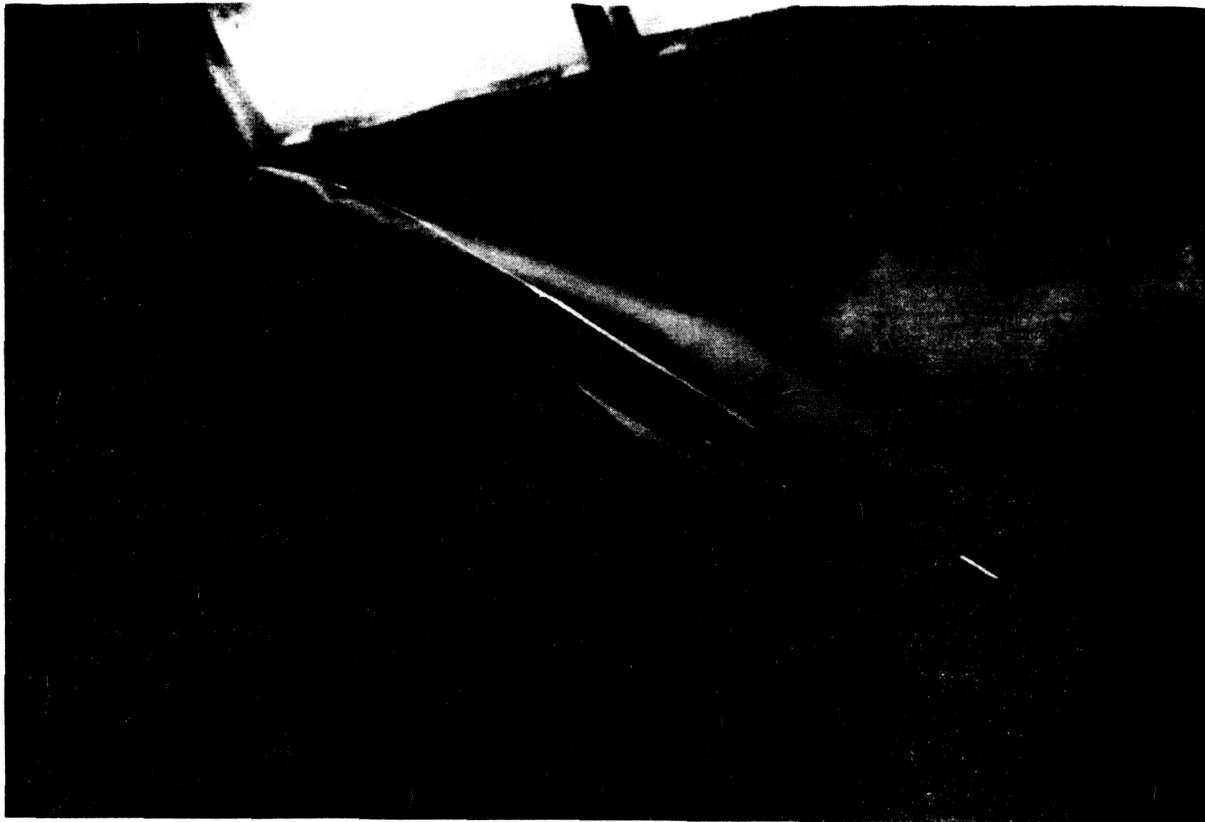
Fig. 30   Smoke flow visualization of chine forebody with 45° (upward) chine deflection; α = 40°.
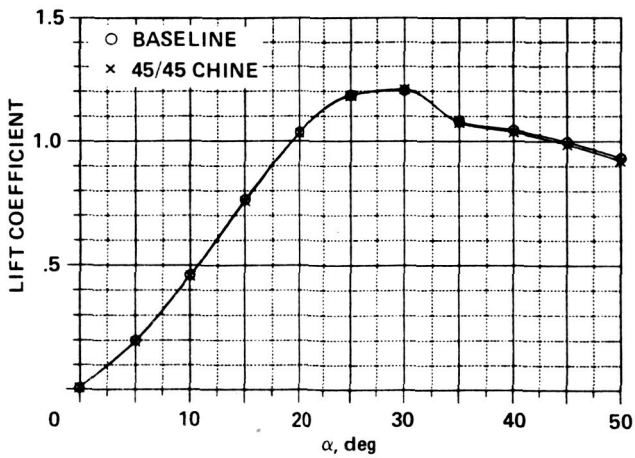
Fig. 31   Effect of 45° (upward) chine deflection on lift.
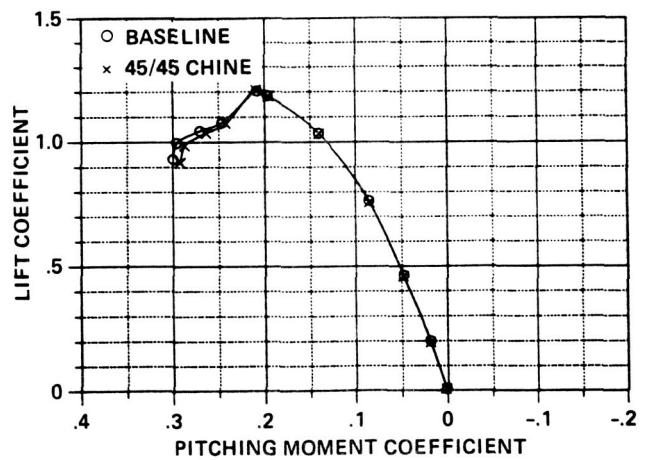

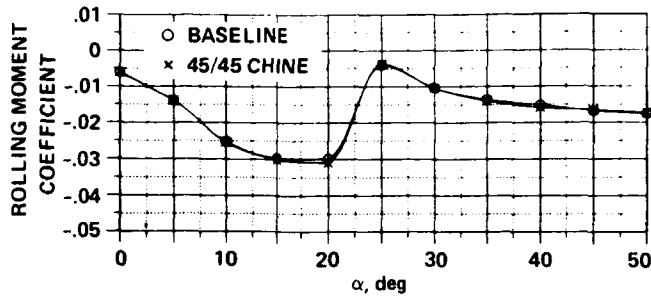Fig. 32   Effect of 45° (upward) chine deflection on pitching moment.

34

Fig. 33 Effect of 45° (upward) chine deflection on rolling moment; β = 10°.

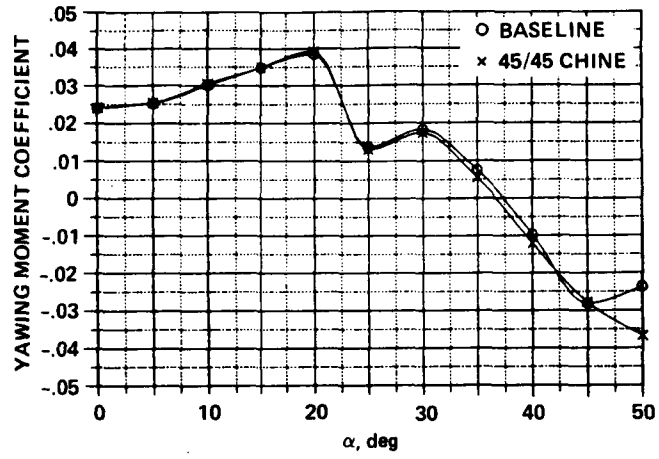Fig. 34 Effect of 45° (upward) chine deflection on yawing moment; β = 10°.

NASA
National Aeronautics and Space Administration

Report Documentation Page

1. Report No. NASA TM 89447	2. Government Accession No.	3. Recipient's Catalog No.
4. Title and Subtitle On the Nonlinear Aerodynamic and Stability Character-istics of a Generic Chine-Forebody Slender-Wing Fighter Configuration		5. Report Date June 1987
		6. Performing Organization Code
7. Author(s) Gary E. Erickson and Jay M. Brandon (NASA Langley Research Center, Hampton, VA)		8. Performing Organization Report No. A-87174
		10. Work Unit No. 505-61-71
9. Performing Organization Name and Address Ames Research Center. Moffett Field, CA 94035		11. Contract or Grant No.
12. Sponsoring Agency Name and Address National Aeronautics and Space Administration Washington, DC 20546		13. Type of Report and Period Covered Technical Memorandum
		14. Sponsoring Agency Code

15. Supplementary Notes

Point of Contact: Gary E. Erickson, Ames Research Center, MS 227-2, Moffett Field, CA 94035, (415)694-6463 or FTS 464-6463

16. Abstract

An exploratory investigation was conducted of the nonlinear aerodynamic and stability characteristics of a tailless generic fighter configuration featuring a chine-shaped forebody coupled to a slender cropped delta wing in the NASA Langley Research Center's 12-Foot Low-Speed Wind Tunnel. Forebody and wing vortex flow mechanisms were identified through off-body flow visualizations to explain the trends in the longitudinal and lateral-directional characteristics at extreme atti-tudes (angles of attack and sideslip). The interactions of the vortical motions with centerline and wing-mounted vertical tail surfaces were studied and the flow phenomena were correlated with the configuration forces and moments. Single degree-of-freedom, free-to-roll tests were used to study the wing rock suscepti-bility of the generic fighter model. Modifications to the nose region of the chine forebody were examined and fluid mechanisms were established to account for their ineffectiveness in modulating the highly interactive forebody and wing vortex systems.

17. Key Words (Suggested by Author(s)) Vortex flows High-angle-of-attack aerodynamics Stability and control	18. Distribution Statement Unlimited – Unclassified Subject Category: 02

19. Security Classif. (of this report) Unclassified	20. Security Classif. (of this page) Unclassified	21. No. of pages 38	22. Price A03